



ELSEVIER

Contents lists available at SciVerse ScienceDirect

## Journal of Sound and Vibration

journal homepage: [www.elsevier.com/locate/jsvi](http://www.elsevier.com/locate/jsvi)

# Investigation of flow features and acoustic radiation of a round cavity

O. Marsden\*, C. Bailly, C. Bogey, E. Jondeau

Laboratoire de Mécanique des Fluides et d'Acoustique, Ecole Centrale de Lyon, UMR CNRS 5509 & Université de Lyon, 36 Avenue Guy de Collongue, 69134 Écully Cedex, France

## ARTICLE INFO

### Article history:

Received 8 December 2010

Received in revised form

3 October 2011

Accepted 13 March 2012

Handling Editor: P. Joseph

Available online 11 April 2012

## ABSTRACT

In this work, the interaction between a boundary layer and a circular cylindrical cavity is studied. Experimental pressure and velocity results for a cavity of diameter 10 cm and depth ranging from 10 to 15 cm are described, for flow velocities between 50 and  $110 \text{ m s}^{-1}$ . This flow configuration is found to generate intense discrete depth- and flow-dependent tones, resulting in modes similar in appearance to Rossiter modes found in shallow rectangular cavities. Differences between the cylindrical cavity's mean flow and that of a similarly sized rectangular cavity are highlighted. The development of the shear layer is quantified, in terms of thickening and of velocity statistics profiles. Radial and azimuthal acoustic modes are observed in the acoustic field inside the cavity. A feedback model based on the coupled behaviour of the fundamental acoustic depth mode of the cavity and the large scale dynamics of the shear layer is constructed, and its response is compared to experimental data. A good qualitative agreement between available data and modeled behaviour is observed, allowing the two acoustic modes found in this work to be attributed to the interaction of the shear layer with the cavity's fundamental depth mode.

© 2012 Elsevier Ltd. All rights reserved.

## 1. Introduction

The noise generated by civil aircraft both in taking-off and in landing phases is currently one of the main aspects limiting traffic growth in large international airports. Among the different causes of total aircraft noise, acoustic radiation due to various elements of the airframe is one of the major sources of community-perceived aircraft noise during the approach configuration [1]. There are many contributors to airframe noise, including for example landing gear and high-lift devices, both of which have been studied in numerous research works. The tonal noise generated by burst-disk cavities and vent holes located under wings has been subject to less investigation, despite being clearly identifiable in fly-over measurements [2] even if there is no direct impact on current certification levels.

Noise generated by rectangular cavities excited by a grazing flow has been the focus of countless studies in aeroacoustics since the 1950s and the pioneering work of Roshko [3] and Karamcheti [4]. Noteworthy general reviews on the subject have been written by Rockwell and Naudascher [5] or Rockwell [6] for instance. It was quickly noted that cavity radiation was often tonal, with one or multiple discrete tones being emitted, and moreover that detailed cavity geometry, as well as precise incoming flow conditions, can have a strong influence both on mean flow inside the cavity and

\* Corresponding author.

E-mail addresses: [olivier.marsden@ec-lyon.fr](mailto:olivier.marsden@ec-lyon.fr), [olivier.marsden@gmail.com](mailto:olivier.marsden@gmail.com) (O. Marsden).

Nomenclature			
$c$	speed of sound	$q_{ac}$	acoustic volume flow through the cavity mouth
$C_p$	mean pressure coefficient, $C_p = (p - p_\infty) / (\rho_\infty U_\infty^2 / 2)$	$q_h$	hydrodynamic volume drive flow generated by shear layer motion
$D$	cavity diameter, $D = 2r_0 = 10$ cm	$r_0$	cavity radius
$f$	frequency	$S$	cavity mouth area $S = \pi r_0^2$
$h$	cavity depth	$U_c$	convection velocity
$H = \delta_* / \delta_\theta$	boundary layer shape factor	$U_\infty$	free stream velocity
$k = \omega / U_c$	hydrodynamic wavenumber	$w_{ac}$	acoustic velocity through the cavity mouth
$k_0 = \omega / c$	acoustic wavenumber	$\delta_*$	displacement thickness
$M = U_\infty / c_\infty$	Mach number	$\delta_\theta$	momentum thickness
		$\delta_h$	cavity depth correction term
		$\xi$	vertical displacement of the shear layer

on the noise radiated by the cavity. Accordingly, a large number of experimental studies have looked into the influence of the cavity dimensions [3,4,7,8], thickness of the incoming boundary layer and its laminar or turbulent state [4,8–10], and Mach number.

One of the first and most well-known explanations of tonal noise generation is due to Rossiter [11]. His extensive experimental campaign showed discrete tones varying in frequency with Mach number and cavity length, and he proposed a semi-empirical model that fitted his observations reasonably accurately. In this model, large vortical structures are created at the leading edge, convected by the shear layer at a certain fraction of the freestream velocity, and impact the downstream cavity edge. The resulting acoustic waves propagate upstream and, for certain wavelengths, synchronise the development of new large-scale vortices, thus creating self-sustaining flow oscillations, similar to the oscillations described and modeled by Powell [12] for jet-edge interactions. This description thus corresponds to a feedback model, with a hydrodynamic forward path and an acoustic backward path, and links the Strouhal number  $St$  of oscillations to an average number  $n$  of discrete vortices in the shear layer, an average convection velocity of large vortical structures in the shear layer  $U_c$  and Mach number  $M$  by

$$St = \frac{fL}{U_\infty} = \frac{n - \alpha}{U_\infty / U_c + M} \quad (1)$$

where  $\alpha$  is a delay term with a value of roughly one quarter, and  $L$  the length of the rectangular cavity.

A number of refinements to Rossiter's model have since been proposed. Some of these modifications are relatively minor, allowing for example to fit tones resulting from supersonic flow speeds [13], or to better describe the effect of the cavity length to depth ratio [14]. Other authors have proposed analytical developments to clarify the role of the shear layer. Bilanin and Covert [15] accounted for the phase of velocity perturbations convected by an infinitely thin shear layer, hoping to find a physical justification for the constants in Rossiter's model. Block [14] proposed to generalise Bilanin's model by accounting for acoustic reflexions on the cavity floor in the acoustic feedback path. In a later work, Tam and Block [7] replaced the vortex sheet assumption previously used by a linear stability analysis on hyperbolic tangent shear layer velocity profiles. They suggested that for lower Mach numbers  $M < 0.2$ , depth modes dominate the acoustic emission of deep cavities, yielding frequencies independent of freestream flow velocity. They also provided experimental results for different cavity depths substantiating this claim. Blake [16] proposed a physical explanation for the commonly observed value of 1/4 for one of the key constants in Rossiter's formula,  $\alpha$  in Eq. (1), linking it to an optimal phase lag of  $\pi/2$  between inflow at the downstream edge and shear layer forcing at the upstream edge.

More recently, Direct Noise Computations have also been realised with success for two dimensional [17,18] and three dimensional configurations [19] by direct numerical simulation and large-eddy simulation, respectively. Investigations of the three-dimensional flow dynamics through large-eddy simulations have also been performed [20] as well as studies of control techniques as a possible means of reducing noise generation [21,22]. Recent syntheses of the extensive literature on this topic can be found in Cattafesta et al. [23] or in Rowley and Williams [24].

Cavities of cylindrical shape have received far less attention from the research community than their rectangular counterparts. Deep cylindrical cavities, such as organ pipes and cavities encountered in hydraulic side-branches, are an exception. Powell [12] first suggested that organ pipe sound production could be due to an edgetone excitation mechanism interacting with a depth-mode resonance. Later researchers developed the idea in more detail, in particular explaining how the resulting pipe frequency was relatively independent of the jet excitation velocity [25,26]. Side branch pipes in hydraulic systems, exhibiting fluid-resonant behaviour, have also been studied in some detail [5]. Experimental and theoretical studies have been performed on various aspects such as the flow velocity required for the onset of oscillations [27–29], nonlinear coupling of acoustic modes [30], and the effect of pipe and branch geometry [31]. However, documentation on shallower cylindrical cavities, with a diameter-to-depth ratio of the order of one, is relatively scarce. Elder [32] studied a cylindrical cavity partially closed by a flat plate with a rectangular opening. Thanks to the simultaneous measurement of hot-wire signals in the shear layer and a pressure signal in the cavity, he was able to

show that the shear layer exhibited a large-scale *interface wave* whose behaviour was well predicted by linear instability theory, despite the turbulent nature of the incoming boundary layer. He then used this to relate both resonant frequencies and resonance amplitude to cavity geometry and flow speed. Parthasarathy et al. [33] examined the sound generated by small cylindrical cavities at relatively low Mach numbers, and found that for his experimental conditions, a strong tonal frequency was generated that varied with the flow speed according to  $f \propto (1-M)^{-1}$ . He was able to match a simple 1D oscillator model to his results, explaining qualitatively the acoustic power output variation as a function of flow velocity. It is interesting to note that these two studies, both performed at relatively low Mach numbers  $M < 0.25$ , provided experimental data showing acoustic frequency varying with flow Mach number, contrary to results shown published by Tam and Block [7] for rectangular cavities of similar aspect ratios.

In the present work, self-sustained flow and acoustic oscillations generated by a turbulent boundary layer grazing a cylindrical cavity set in a flat plate are investigated experimentally. This configuration is currently being studied by a number of research teams working with numerical simulations to document cylindrical cavity acoustics [34–36]. Such cavities are found on the pressure side of civil aircraft wings in the form of kerosene over-pressure vents. Therefore, an attempt is made to provide a reference test case with flow and geometric parameters adapted to this aeronautical context, for which numerous and varied experimental results are described. The turbulent flow around a 10 cm diameter cavity and its acoustics are characterised for a depth-to-diameter ratio between 1 and 1.5, and freestream velocities in the range of 50–110 m s<sup>-1</sup>. Strong tonal peaks are observed in the far acoustic field. Peak frequencies vary both with flow velocity and with cavity depth. Acoustic behaviour is found to be well described by an acoustic depth-mode resonance excited by shear layer instabilities. A symmetrical but highly 3D mean flow is observed from static pressure measurements inside the cavity. Internal radial and azimuthal cavity modes are found to be excited, but they are not radiated to the far field. A model proposed by Elder [32], adapted here for cylindrical cavities, is then used to discuss acoustic results. A good match between frequencies observed in experiments and those predicted by the model is found, suggesting that feedback between large-scale shear layer oscillations and the cavity depth mode is responsible for the tonal acoustic emission observed in this study.

## 2. Experimental setup and techniques

### 2.1. ECL facility

The experiments were conducted in the main subsonic wind tunnel of the Centre Acoustique at the Ecole Centrale de Lyon (ECL) in France. The flow is generated by a 350 kW Neu centrifugal blower delivering a nominal mass flow rate of 15 kg s<sup>-1</sup>, and the fan is powered by an electronically controlled Tridge-Electric LAK 4280A motor. Air passes through a settling chamber as well as through a honeycomb and several wire meshes designed to reduce free stream turbulence. Acoustic treatment on the wind tunnel walls and baffled silencers allow flow noise levels and contamination of the acoustic measurements performed in the anechoic chamber to be kept to a minimum. As shown in Fig. 1, the flow is finally guided into a large anechoic room of 10 × 8 × 8 m<sup>3</sup>, by a rectangular nozzle with a cross-section of 0.5 by 0.25 m over a flat plate measuring 0.8 m in the streamwise direction by 0.6 m in the cross-flow direction, thus forming a rectangular-section wall jet. The round cavity of radius  $r_0 = 50$  mm is placed 450 mm downstream from the nozzle exit, well inside the potential core of the wall jet. Fig. 2 provides a schematic view of the setup and coordinate system. In order to obtain a reproducible turbulent incoming boundary layer, a strip of sandpaper is placed inside the nozzle before the convergent zone, thus ensuring a complete transition to a turbulent state for all flow velocities of interest. The main flow and geometric parameters of the study are listed in Table 1. The main part of the study deals with a cavity depth of 100 mm, but depths of up to 150 mm are also considered.

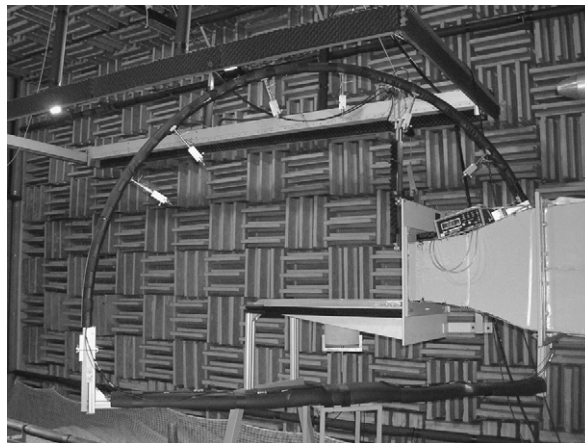


Fig. 1. Picture of the experimental setup in the ECL anechoic wind tunnel including the semi-circular rotating antenna of microphones.

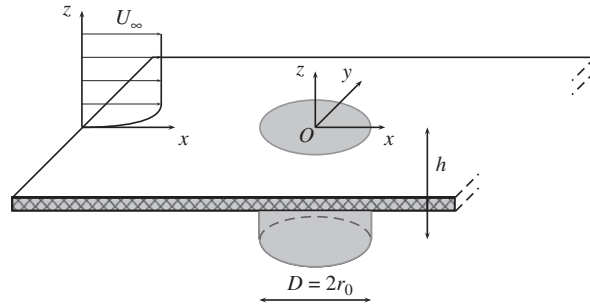


Fig. 2. Schematic view of the round cavity and the Cartesian coordinate system.

**Table 1**

Main parameters of the flow configurations studied. The Reynolds number based on the cavity diameter lies in the range  $3.3 \times 10^5 \leq Re_D \leq 7.3 \times 10^5$ .

Cavity radius $r_0$	50 mm
Cavity depths $h$	100, 125, 150 mm
Flow velocities $U_\infty$	50–110 m s <sup>-1</sup>
Boundary layer thickness $\delta_{99}$	17 mm

## 2.2. Pressure measurements

The cavity has been instrumented in order to allow the measurement of both static and fluctuating wall pressure. For static wall pressure measurements, 0.7 mm stainless steel tubes are flush-mounted on the cavity walls, and connected to a Furness manometer using atmospheric pressure as reference. These pressure tappings are located along four vertical lines on the cylindrical wall, and along two perpendicular diameters on the cavity floor. The cavity block can be rotated with respect to the grazing flow, allowing the static pressure to be measured at any angular position around the cavity. In a similar way, the cavity can be fitted with a total of 20 $\frac{1}{4}$ " Brüel and Kjær Type-4935 microphones, arranged in four vertical lines comprising of four microphones each, and four microphones on the cavity floor. Again, the instrumented cavity can be rotated with respect to the flow in order to obtain fluctuating pressure measurements anywhere on the cavity walls. Far-field acoustic directivity measurements have also been performed, thanks to seven Brüel and Kjær ICP type 4935 microphones placed on a semi-circular rotating antenna of radius 1 m centred on the middle of the cavity opening.

## 2.3. Characterisation of turbulent velocity fields

Turbulent velocity fields have mainly been obtained by time resolved particle image velocimetry (TR-PIV). The CMOS camera used in the present TR-PIV system is a Phantom V12 with a resolution of 1280 × 800 pixels and a dynamic range of 12 bits. The camera was inclined by an angle of 7° with respect to the flat plate, in order to obtain a 100 × 60 mm<sup>2</sup> window of the shear layer above and just under the cavity opening. Images were corrected for the resulting optical distortion. The light sheet was provided by a Quantronix Darwin Duo Nd:YLF dual-cavity laser with a pulse energy of 18 mJ and a 527 nm wavelength. A data set consists of 2700 pairs of images, obtained at a repetition rate of 3000 Hz in the present experiments. A total of six data sets were recorded during the experimental campaign. The laser and camera synchroniser are triggered by a microphone signal of the sound field radiated by the cavity. LaVision DaVis v7.2 software is used to compute flow fields from pairs of images by multipass correlation. A pass subregion size of 128 × 128 pixels is first considered. The interrogation window is then reduced to 16 × 16 pixels with 50 percent overlap. Finally to seed the flow field, a SAFEX smoke generator was used to create glycol particles of size 1 μm.

Hot-wire anemometry has also been used both to validate PIV data and to characterise the incoming boundary layer. The hotwire data was obtained using a Dantec model 55p11 with a 5 μm diameter, 1.25 mm long platinum-plated tungsten wire. The hotwire was operated at an overheat ratio of 0.8 and was controlled by a Dantec Streamline 90C10 module. The hotwire signal was digitised at 10 kHz and 24 bits resolution using a PXI-4472 system. An anti-aliasing filter was applied to the hotwire signal before its digitisation.

## 2.4. Incoming mean flow

Flow velocity ranges from 50 to 110 m s<sup>-1</sup>, or approximately  $M=0.15$  to  $M=0.34$ . The boundary layer thickness  $\delta_{99}$ , also reported in Table 1, varies between around 18 mm and 16 mm over this Mach number range, while the shape factor remains approximately constant at  $H \approx 1.35$ . Turbulence levels in the free stream are low, and do not exceed 1 percent of

the freestream velocity. Maximum fluctuation levels in the boundary layer are recorded at a distance of approximately 3 mm from the wall, but this distance is probably overestimated due to the hot-wire setup used for performing the measurements. Mean and rms fluctuation velocity profiles for the  $70 \text{ m s}^{-1}$  case, measured 225 mm upstream of the cavity leading edge by HWA, are shown in Fig. 3, in (a) physical units on the left and (b) wall units on the right. From the representation scaled in wall variables, a strong wake component is observed in the velocity profile, which may be due to the nonconfined nature of the wall-jet flow. Velocity profiles have also been measured at different values of the cross-stream  $y$  coordinate to ensure that the boundary layer is relatively two-dimensional upstream of the cavity. Profiles of streamwise velocity, not represented, display reasonable similarity, with differences not exceeding  $4 \text{ m s}^{-1}$  throughout the boundary layer. The transversal velocity component also remains small, not exceeding  $3 \text{ m s}^{-1}$  at any of the measurement locations.

### 3. Experimental results

In this section, acoustic results measured in the far field above the cavity are first reported. The flow field in the shear layer and inside the cavity are then described, based on velocity and static wall pressure measurements.

#### 3.1. Acoustic trends

General properties of the far acoustic field are first described. An estimate of the acoustic output as a function of velocity is presented in Fig. 4(a). The power of the acoustic signal measured at a distance of 1 m directly above the cavity is represented over the range  $U_\infty = 50 \text{ m s}^{-1}$  to  $U_\infty = 110 \text{ m s}^{-1}$ , for a cavity depth of  $h=100 \text{ mm}$ . It can be seen to increase from 79 dB for an upstream flow velocity of  $50 \text{ m s}^{-1}$ , to 104.5 dB at  $110 \text{ m s}^{-1}$ , with a local maximum of 95.5 dB at  $70 \text{ m s}^{-1}$ . It is compared to a  $U_\infty^6$  evolution, represented by the dashed line, scaled to correspond to the experimental power level at  $50 \text{ m s}^{-1}$ . Acoustic scaling based on  $U_\infty^6$  is typical of compact dipolar noise source mechanisms, such as turbulent fluctuations close to a rigid surface. Thus a sixth power scaling could be anticipated in the absence of notable acoustic resonance or feedback in the cavity, as a result of the shear layer interaction with the downstream cavity wall. While the  $U_\infty^6$  scaling matches the minima of the acoustic power evolution quite well, notable deviations are visible for velocities around  $70 \text{ m s}^{-1}$  and around  $100 \text{ m s}^{-1}$ . In Fig. 4(b), a spectral representation of the pressure signals is given for

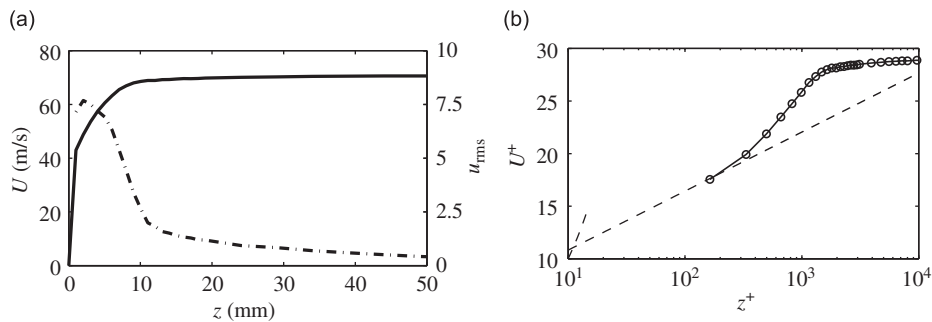


**Fig. 3.** Case  $U_\infty = 70 \text{ m s}^{-1}$ . (a) Solid black line: boundary layer profile 225 mm upstream of the cavity, as a function of  $z$ . Dashed black line: profile of rms fluctuations as a percentage of  $U_\infty$  in the boundary layer, as a function of  $z$ . (b) Symbols: velocity profile represented in wall units, dashed line: standard log law.

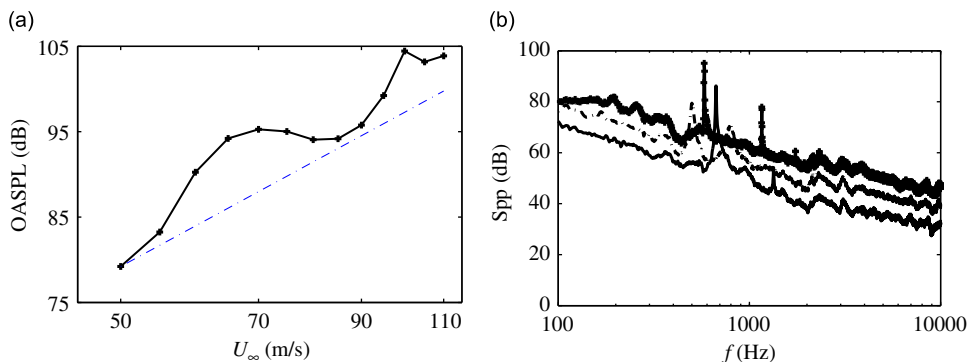


**Fig. 4.** (a) Experimental acoustic power level in dB at 1 m above the cavity, as a function of freestream velocity. - - - - experimental data, - - -  $U_\infty^6$  scaling law. (b) Power spectral density at 1 m above the cavity, for 70 in solid line, 90 in dashed line and  $110 \text{ m s}^{-1}$  - - - -.

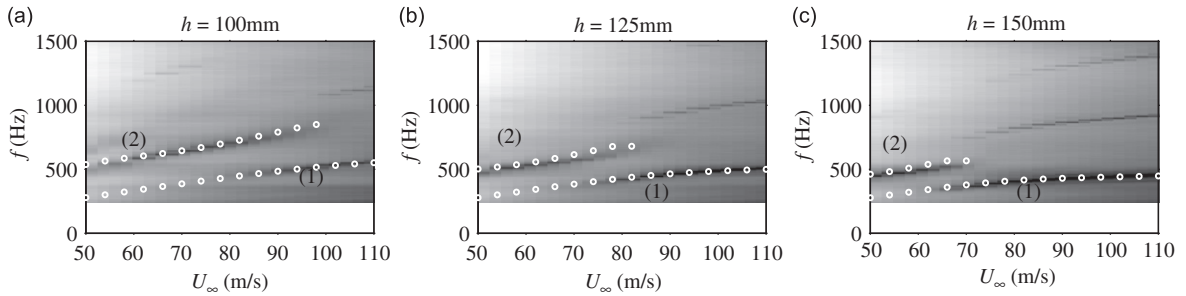


**Fig. 5.** Acoustic power spectral density (PSD) at 1 m above the cavity as a function of freestream velocity, for (a)  $h=100$  mm, (b)  $h=125$  mm, (c)  $h=150$  mm. Gray scale between 30 and 100 dB. The white circles correspond to the solution of Eq. (7), where the two transfer functions are given by (5) and (6).

three freestream velocities, namely 70, 90 and  $110 \text{ m s}^{-1}$ . The 70 and  $90 \text{ m s}^{-1}$  flow speeds exhibit a single sharp peak in their spectra, while the flow speed of  $90 \text{ m s}^{-1}$  generates two smaller peaks in the far field. At  $70 \text{ m s}^{-1}$  the peak is found at a frequency of 660 Hz, about 10 percent above the acoustic depth resonance frequency, and this frequency emerges from the broadband noise by around 27 dB to reach a level of 87 dB. Its first harmonic is also distinctly visible, at a frequency of 1320 Hz. The two distinct peaks at  $90 \text{ m s}^{-1}$ , occur at frequencies of 500 Hz and 795 Hz. The lower frequency peak is slightly more intense, reaching a maximum of 80 dB, while the higher frequency peak reaches 72 dB. Neither of the two peaks exhibits discernible harmonics. Finally the  $110 \text{ m s}^{-1}$  flow velocity results in a single intense acoustic peak at a frequency of 580 Hz. The peak has a considerably higher quality factor than that observed at  $70 \text{ m s}^{-1}$ , and emerges from the background noise by more than 30 dB to reach a maximum of 96 dB. Its first harmonic at 1180 Hz is also very pronounced, with an emergence of 18 dB, and the second and even third harmonics are noticeable in the experimental PSD.

The spectral content of the acoustic far field is represented as a function of flow velocity in Fig. 5 for cavity depths of 100, 125 and 150 mm. A number of discrete peaks are seen to emerge from the base noise level, providing a pattern similar to those observed in many studies focusing on rectangular cavities. The peaks' frequencies increase with flow velocity, in a roughly linear fashion over the range of velocities studied here, giving rise to acoustic modes in the far field. This is different from the tonal behaviour of deeper rectangular cavities, such as those examined by Yang et al. [37] who found that for the cavities of length-to-depth ratio of 1/7 and smaller, observed frequencies were independent of flow velocity. Tam and Block [7] also found tonal behaviour to be independent of flow velocity for rectangular cavities of similar length-to-depth ratios at low Mach numbers  $M < 0.2$ .

The level of total radiated noise increases with depth. For a depth of  $h=100$  mm, two main modes are clearly visible, and are of similar amplitude. The first mode goes from a frequency of 500 Hz at a flow velocity of  $50 \text{ m s}^{-1}$  to 850 Hz at  $100 \text{ m s}^{-1}$ , while the second goes from 450 Hz at  $80 \text{ m s}^{-1}$  to 570 Hz at  $110 \text{ m s}^{-1}$ . For depths of  $h=125$  mm and  $h=150$  mm, both modes drop in frequency. The higher-frequency mode (2) migrates towards lower velocities and diminishes in strength, while the lower-frequency mode (1) increases in intensity and extends towards lower velocities. Harmonics of mode (1) are present at all depths. For the 100 mm cavity, only the first harmonic is visible, and only at flow speeds above  $100 \text{ m s}^{-1}$ . As the cavity depth is increased, the second and third harmonics appear, and are present at lower flow speeds down to  $75 \text{ m s}^{-1}$  for  $h=150$  mm.

### 3.2. Flow inside the cavity

It is not easy to measure mean flow properties in the cavity interior, because of the cavity's cylindrical geometry. Nevertheless, two-component U-V LDA measurements inside the cavity have been performed in the  $y=0$  plane, and static pressure has been measured on the cavity walls.

The mean and fluctuating streamwise velocity inside the cavity is illustrated in Fig. 6(a) and (b). These measurements show a large recirculation whose centre is located in the bottom half of the cavity, similar to what is observed for square-section cavities at moderate Reynolds numbers [38]. The recirculating flow along the floor of the cavity is intense, reaching  $18 \text{ m s}^{-1}$  at  $x=0$  and  $z=-98$  mm. This strong wall shear is enough to generate intense turbulent fluctuations, reaching r.m.s levels of 35 percent of the local mean velocity at the same measurement location.

The static pressure distribution on the cavity wall can also give useful insight into the behaviour of the mean flow, and in particular its differences with respect to better known rectangular cavity flows. The pressure coefficient  $C_p$  on the cavity wall and floor for a flow velocity of  $70 \text{ m s}^{-1}$  is shown in Fig. 7. The pressure distribution is almost, but not exactly, symmetrical with respect to the flow direction. For smaller depth-to-diameter ratios around 0.5, it has been shown that a strongly asymmetric mean flow can be generated [39–41] but such phenomena have not been observed for a depth-to-diameter ratio of one, as in this work. The slight asymmetry is presumed to stem from an imperfect alignment in the experimental set-up, but its origin has not been investigated further, since it is almost everywhere inferior to 5 percent of the  $C_p$  values. The impact zone of the shear layer on the downstream wall is clearly visible, corresponding to the zone of positive  $C_p$  centred around the polar angle  $\theta=0$  indicating the downstream direction. It is substantially lower than for rectangular cavities with similar length-to-depth ratios and Mach numbers, where the  $C_p$  in the impact zone is typically around

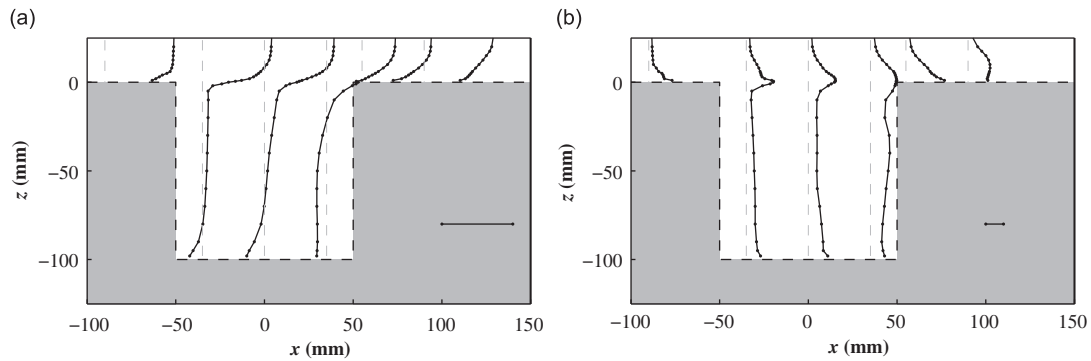


**Fig. 6.** Mean streamwise velocity (a) and rms streamwise velocity (b) measured by LDA in the  $y=0$  plane of the cavity. Freestream flow velocity of  $70 \text{ m s}^{-1}$ . Bar lengths in the bottom right of each plot correspond to (a)  $U_\infty$  and (b) 7 percent, that is the maximum turbulence level measured in the upstream boundary layer.

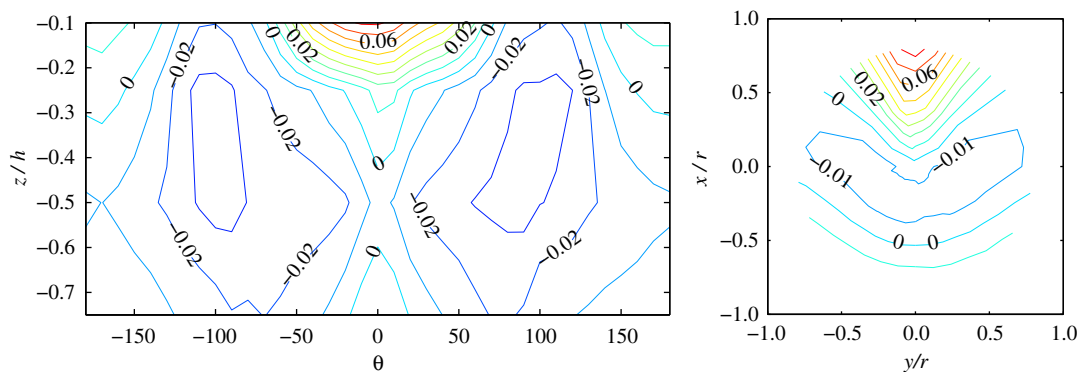


**Fig. 7.** Mean pressure coefficient  $C_p$  on the cavity wall and floor as a function of the polar angle  $\theta$ , where  $\theta = 0^\circ$  designates the downstream direction. Freestream flow velocity of  $U_\infty = 70 \text{ m s}^{-1}$ .

0.3–0.4. This impact generates a general downward motion along the downstream vertical edge, and creates a large central recirculation zone, rotating around an axis aligned with the cross-flow  $y$  direction, and whose shape is skewed slightly due to the round geometry of the cavity. Its  $C_p = 0$  trace on the cavity floor has a characteristic horseshoe shape, as also seen in results from [39,40]. Along the upstream bottom edge, there are signs of a smaller counter-rotating recirculation, as often seen in rectangular cavities. Unlike in rectangular cavities, however, where this counter-rotating recirculation is mostly aligned with the cross-flow direction, here the vortex geometry is constrained by the circular cavity wall, yielding a crescent-like shape visible in its contact zone of positive  $C_p$  on the floor, which extends around  $90^\circ$  to each side of the  $\theta = 180^\circ$  direction. Similar pressure distributions are observed for velocities over the range  $50 \leq U_\infty \leq 110 \text{ m s}^{-1}$ .

### 3.3. Upstream boundary layer characteristics

Flow features around the cavity are studied by LDA and HWA in the upstream boundary layer and by PIV in the shear layer above the cavity. It has been shown in a number of past studies that the properties of the incident boundary layer exert a decisive influence on the presence, frequency and amplitude of cavity oscillations. For the present study, these parameters are as follows. The boundary layer thickness measured 225 mm upstream of the cavity by hot wire anemometry is found to be  $\delta_{99} = 17 \text{ mm}$  and the momentum thickness,  $\delta_\theta = 1.8 \text{ mm}$ . This yields a ratio of cavity diameter to momentum boundary layer thickness of  $D/\delta_\theta = 55$ , and a diameter to boundary layer thickness of  $D/\delta_{99} = 5.9$ . The second ratio is substantially smaller than the minimum value of  $L/\delta_{99} > 15$  proposed by Ahuja and Mendoza [8], under which shallow 2D rectangular cavities grazed by a turbulent incident boundary layer should not generate oscillations.

### 3.4. Shear layer characteristics

Flow field features in the shear layer were investigated by PIV. Fig. 8 presents the mean streamwise  $U$  and vertical  $W$  velocity fields in the  $y=0$  plane of symmetry, while rms values of the corresponding fluctuating fields are shown in Fig. 9. The upper extremity of the cavity recirculation is visible in particular on the mean  $W$  component shown in Fig. 8(b), with a wide upward movement of between 2 and  $5 \text{ m s}^{-1}$  over the first two thirds of the cavity opening, and a more localised and stronger downward motion of around  $5 \text{ m s}^{-1}$  near the cavity's downstream edge. From Fig. 8(a), it can be seen that over

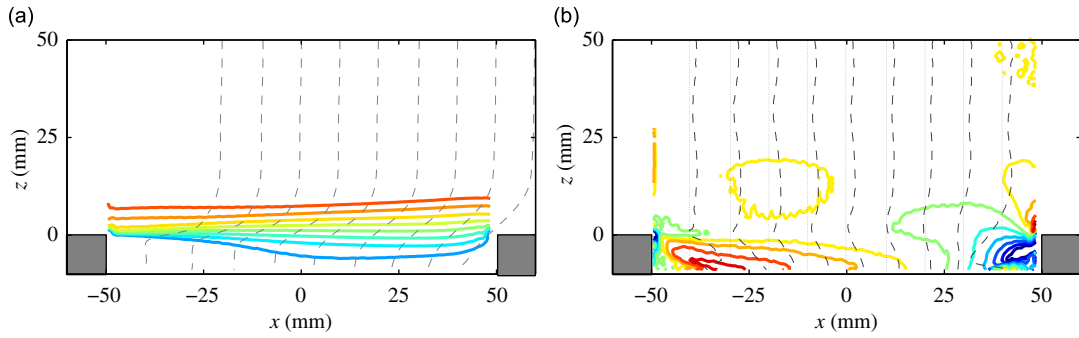


**Fig. 8.** Mean  $U$  (a) and  $W$  (b) velocity components in the shear layer above the cavity at  $y=0$  at a freestream flow velocity of  $70 \text{ m s}^{-1}$ . Contour lines for (a) from 20 to 90 percent of  $U_\infty$  by steps of 10 percent, contour lines for (b) from  $-5$  to  $5 \text{ m s}^{-1}$  by steps of  $1 \text{ m s}^{-1}$ .

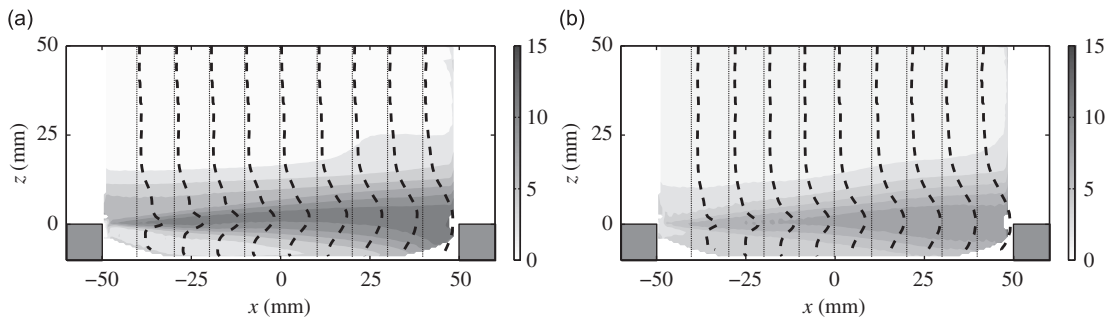


**Fig. 9.** Fluctuating  $u'_{rms}$  (a) and  $w'_{rms}$  (b) velocity components as a percentage of  $U_\infty$  in the shear layer above the cavity at  $y=0$  at a freestream flow velocity of  $70 \text{ m s}^{-1}$ .

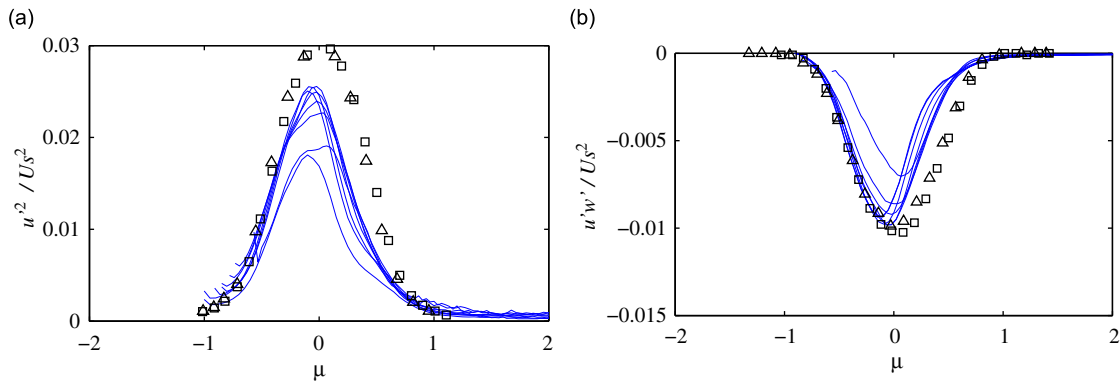


**Fig. 10.** Scaled Reynolds-stress profiles as a function of scaled cross-stream coordinate. Symbols: experiment of Bell and Mehta [44], solid lines taken at different streamwise positions. (a)  $\langle u'^2 \rangle / U_s^2$  and (b)  $u'w' / U_s^2$ , where  $U_s = U_o - U_i$  and  $U_i$  is the velocity underneath the shear layer, and are represented as a function of the cross-stream  $z$  coordinate scaled as  $\mu = (z - z_{50}) / (z_{90} - z_{10})$  where  $z_\alpha$  is such that  $\langle U(x, 0, z_\alpha(x)) \rangle = U_i + \alpha(U_o - U_i)$ . Reasonable self-similarity is found for profiles of both quantities in the

most of the cavity diameter, the mean streamwise velocity just under the shear layer is between  $10$  and  $15 \text{ m s}^{-1}$ , or between  $14$  and  $21$  percent of the freestream velocity.

Maximum fluctuation levels of up to  $13$  percent of the freestream velocity for  $u'$  and  $10$  percent for  $w'$  are observed in the shear layer, as seen in Fig. 9(a) and (b). For laminar incoming boundary layers, Sarohia [42] observed maximum  $u'$  levels in the shear layer above rectangular cavities of around  $15$  percent, while in the case of turbulent incoming boundary layers, observed maxima vary from around  $17$  percent [43] to roughly  $25$  percent [10]. Profiles of  $u'$  are seen to change progressively from a characteristic boundary layer shape with a maximum very close to  $z=0$ , to a shape and indeed amplitude similar to those found in free mixing layers [44]. To illustrate this point more quantitatively, Fig. 10 represents scaled Reynolds-stress profiles as a function of the scaled cross-stream coordinate. Both the  $\langle u'^2 \rangle$  and  $\langle u'w' \rangle$  profiles are scaled by the square of the velocity difference across the shear layer,  $U_s = U_o - U_i$ , where  $U_o$  is the local mean velocity outside the shear layer and  $U_i$  the velocity underneath the shear layer, and are represented as a function of the cross-stream  $z$  coordinate scaled as  $\mu = (z - z_{50}) / (z_{90} - z_{10})$  where  $z_\alpha$  is such that  $\langle U(x, 0, z_\alpha(x)) \rangle = U_i + \alpha(U_o - U_i)$ . Reasonable self-similarity is found for profiles of both quantities in the

second half of the cavity mouth, over the range  $0 \leq x \leq 33$  mm. Reynolds-stress levels are close to those measured by Bell and Mehta in free shear layers [44].

From the mean flow field measured by PIV, the streamwise growth rate of the shear layer can be estimated in the  $y=0$  plane. It is represented for momentum thickness

$$\delta_\theta = \int \frac{\rho U - (\rho U)_i}{(\rho U)_o - (\rho U)_i} \left[ 1 - \frac{\rho U - (\rho U)_i}{(\rho U)_o - (\rho U)_i} \right] dz$$

and also for vorticity thickness

$$\delta_\omega = \frac{U_s}{\max(dU/dz)}$$

in Fig. 11(a) and (b), respectively. As can be seen from the mean velocity field shown in Fig. 8, the lower boundary of the recorded flow field is very close to the lower edge of the shear layer. A direct calculation of the momentum thickness  $\delta_\theta$  from the measured mean field would thus be prone to a bias dependent on the streamwise  $x$  position. In order to avoid this, for each streamwise location  $x$ ,  $U(x,z)$  is fitted by a function  $f(z) = a + b \tanh(cz)$ , and the momentum-based thickness  $\delta_\theta$  is obtained from functions  $b(x)$  and  $c(x)$ .

For the vorticity-based thickness,  $U_s$  should be defined as the local difference between flow speed above and below the shear layer,  $U_s = U_o - U_i$ , but here we take  $U_s = U_o$  for simplicity. It can be noted that this leads to an error which depends on the streamwise  $x$  position, since  $U_i$  is seen to vary in Fig. 8(a). Based on  $\delta_\theta$ , the growth rate exhibits two distinct zones, a first zone extending from the leading edge to roughly  $x = -0.03$  m where the shear layer thickens rapidly at a rate of  $d\delta_\theta/dx = 0.0515$ , and then a second zone that ends 1 cm from the downstream edge, where the growth rate is limited to  $d\delta_\theta/dx = 0.0292$ . Based on  $\delta_\omega$ , two regions are again observed, the first extending to  $x = -0.02$  m with a growth rate of  $d\delta_\omega/dx = 0.261$  and the second with a growth rate of  $d\delta_\omega/dx = 0.146$ . The second zone corresponds approximately to the region in which fluctuation profiles are self-similar. These growth rates can be compared to measurements performed on a variety of rectangular cavities. Forestier et al. [45] studied a deep rectangular cavity grazed by a turbulent boundary layer at a Mach number of 0.8, and found an established growth rate of  $d\delta_\theta/dx = 0.042$ . Sarohia studied laminar cavity flows at lower Reynolds numbers [42], and found a maximum value of  $d\delta_\theta/dx = 0.022$ .

### 3.5. Coherent structures in the shear layer

An investigation of the existence of large structures in the shear layer is performed by computing spatial two-point correlations of the streamwise and vertical velocity fluctuations. Normalised correlations are computed as

$$R_{u_i u_j}(x_o, z_o, x, z) = \frac{\langle u_i'(x_o, z_o) u_j'(x, z) \rangle}{\sqrt{\langle u_i'^2(x_o, z_o) \rangle \langle u_j'^2(x, z) \rangle}}$$

and the ensemble averaging is performed on a total of 16200 PIV images issued from six consecutive runs. Normalised spatial correlations of  $u'u'$  and  $w'w'$  are shown in Fig. 12(a) and (b), respectively, for  $z_o = 0$  and values of  $x_o$  ranging from  $x_o/r_o = -0.65$  to  $x_o/r_o = 0.85$ . The streamwise velocity correlation exhibits a main peak with an elongated ellipsoidal shape, consistent with measurements performed in incompressible free shear layers [46]. Interestingly, for negative values of  $x_o$ , a secondary peak in the correlation is visible almost exactly 50 mm downstream of the main peak. In the vicinity of its maximum, the cross-stream  $w'w'$  correlation shows a good quantitative agreement with measurements performed by Olsen et al. [46]. The shape of the maximum is again elliptical, but oriented vertically rather than horizontally as for  $u'u'$ , and upstream and downstream of the maximum, characteristic negative lobes associated with large-scale spanwise structures in sheared flow are observed. In the second half of the shear layer, a marked correlation of wavelength 50 mm is observed. For  $x_o/r_o = 0.85$  the correlation between

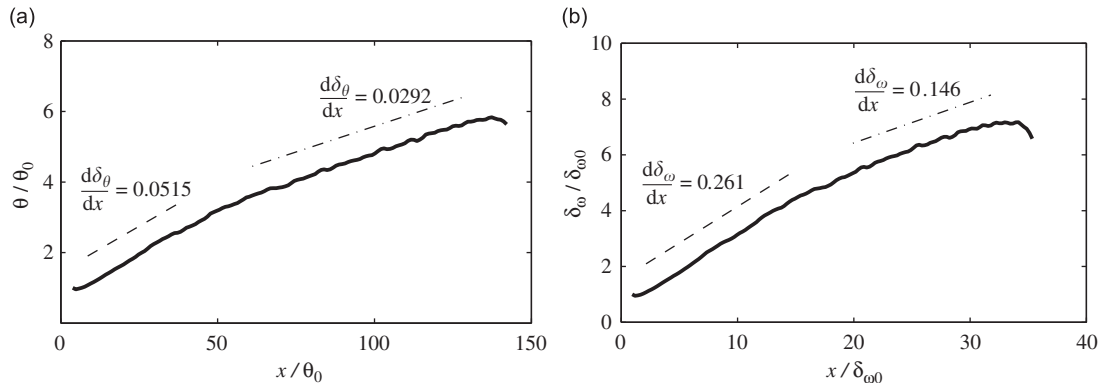
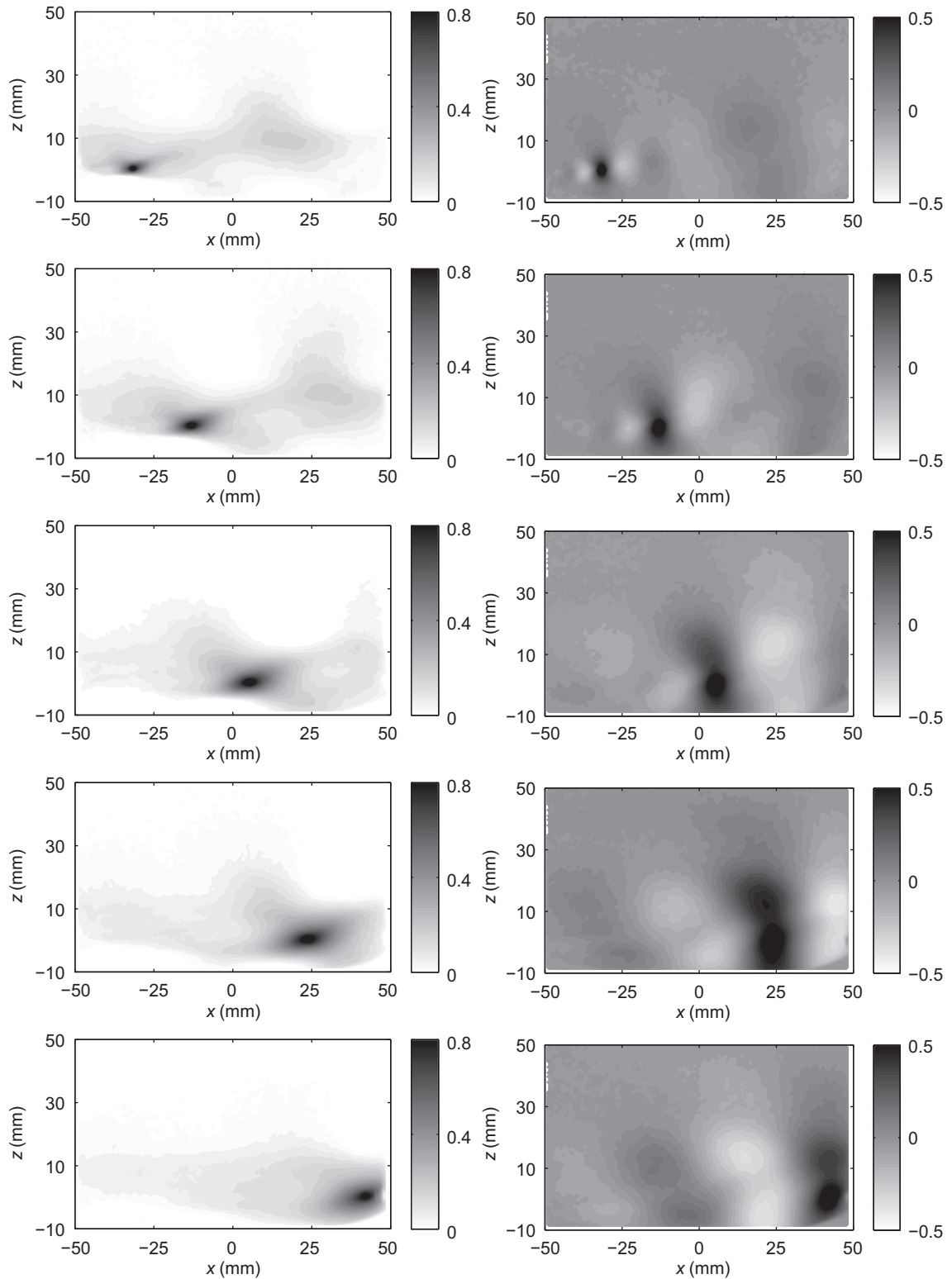


Fig. 11. Shear layer growth rate based on (a) momentum thickness and (b) vorticity thickness. Freestream flow velocity of  $U_\infty = 70$  m s<sup>-1</sup>.



**Fig. 12.** Spatial  $R_{u'u'}$  (left) and  $R_{w'w'}$  (right) velocity correlation functions in the cavity shear layer. Freestream flow velocity of  $70 \text{ m s}^{-1}$ .

$(x_0, z_0)$  and  $(x_0 - 50, z_0)$  reaches a value of 0.14. This value of 0.14 is larger than it might appear at first sight, due to the spatial variation of  $\langle w'^2 \rangle$  along the turbulent shear layer. This suggests an average of two large-scale structures present at any one time in the shear layer, value which will be discussed in Section 4.

### 3.6. Wall pressure fluctuations

Inside the cavity, wall pressure fluctuations have two origins. Firstly, there are fluctuations of a hydrodynamic nature, due both to the impact of the shear layer on the downstream cavity wall, and to the strong, turbulent, recirculation present inside the cavity. Secondly, there are resonant fluctuations linked to the geometry of the cavity. For an open-closed cylindrical cavity of radius  $r_0$  and depth  $h$  placed in an infinite flat plate, the velocity potential for an acoustic cavity mode can be written as [47]

$$\psi_{ijk}(r, \theta, z) = J_j(\lambda_{jk}r/r_0)\cos\left(\frac{i\pi z}{2h}\right)\sin(j\theta + \psi)$$

where  $i=0, 1, 3, \dots$  is the number of quarter-wavelengths in the depth direction,  $j=0, 1, 2, \dots$  is the number of nodal diameters,  $J_j$  the associated Bessel function of the first kind,  $k=0, 1, 2, \dots$  is the number of nodal circles,  $h' = h + 0.8216r_0$  is the effective acoustic depth including the length correction due to the infinite flange for low frequencies [48], and  $\psi$  an arbitrary phase term. The resulting resonant cavity mode frequencies are written as

$$f_{ijk} = \frac{c}{2\pi} \left( \frac{\lambda_{jk}^2}{r_0^2} + \frac{i^2\pi^2}{4h'^2} \right)^{1/2}$$

Values of  $\lambda_{jk}$  and frequencies of interest for the cavity in this work are presented in Table 2.

#### 3.6.1. $U_\infty = 70 \text{ m s}^{-1}$ flow speed

Some of these cavity modes are visible in the power spectral densities of wall pressure signals shown in Fig. 13, which represents PSDs as a function of polar angle  $\theta$ . These measurements were performed using 20 quarter-inch Brüel and Kjær microphones, and time signals acquired by a National Instruments PXI over 64 s at a sampling frequency  $f_s = 12.8 \text{ kHz}$ . Power spectral densities were directly computed by the spectral analyser using a Hanning weighting and 500 samples. Firstly, the impact zone of the unsteady shear layer, along with the downward-oriented wall jet which it generates along the downstream cavity wall, can clearly be seen stretching roughly  $55^\circ$  to each side of the flow direction. It is characterised by its wide-band nature, with a high level of fluctuations up to a frequency of around 3.5 kHz. It is not quite symmetrical with respect to the flow direction, as was previously observed with the static wall pressure, but the asymmetry is again slight. For angles greater than  $65^\circ$ , the spectra are essentially unaffected by the shear layer impact, and the remaining peaks are of acoustic origin. There is a very intense peak at 656 Hz, which is visible for all angles, and which corresponds to the strong tonal frequency observed in the acoustic far field in Fig. 5(a). The peak in the wall-pressure spectra is more intense in the shear impact zone than elsewhere, suggesting that the shear layer is also marked by this frequency.

The dotted black line in Fig. 13 at 608 Hz corresponds to the corrected depth mode  $f_{100}$  with no azimuthal or radial contributions. The + symbol corresponds to the first two azimuthal modes combined with the first depth mode,  $f_{110}$  and  $f_{120}$ . The spectra vary little with depth inside the cavity, both in terms of general level and in terms of shape. A lower frequency peak can also be observed at around 395 Hz. It is more noticeable in the shear layer impact zone, reaching a level of 113 dB, but is also present at lower levels outside of the impact zone.

**Table 2**  
First resonant frequencies  $f_{ijk}$  of a cylindrical open-closed cavity of depth  $h = 10 \text{ cm}$ .

$\lambda_{jk}$	$j=0$	1	2	3
$k=0$	0	1.8412	3.0542	4.2012
1	3.8317	5.3314	6.7061	8.0152
$f_{010} = 2.01 \times 10^3 \text{ Hz}$ $f_{001} = 4.18 \times 10^3 \text{ Hz}$ $f_{011} = 5.82 \times 10^3 \text{ Hz}$				
$f_{100} = 608 \text{ Hz}$ $f_{110} = 2.1 \times 10^3 \text{ Hz}$ $f_{120} = 3.39 \times 10^3 \text{ Hz}$ $f_{101} = 4.23 \times 10^3 \text{ Hz}$				

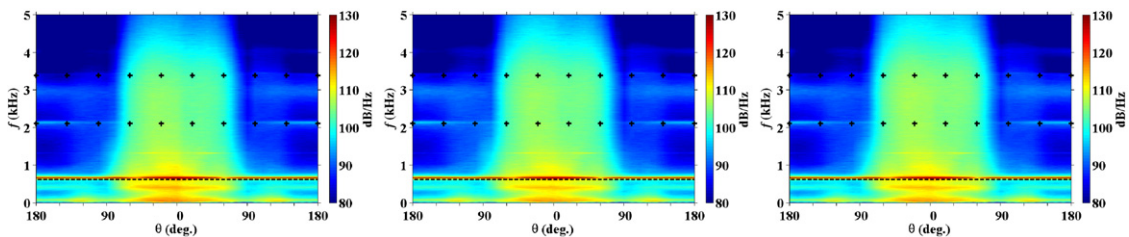


**Fig. 13.** Fluctuating wall-pressure spectra measured at  $z = -0.1, -0.5,$  and  $-0.75 h$  along the circumference inside the cavity as a function of the polar angle  $\theta$ , where  $\theta = 0^\circ$  designates the downstream direction. Acoustic cavity modes are indicated by  $- - -$  for the first depth mode  $f_{100}$  and  $+$  for combined azimuthal and depth modes  $f_{110}$  and  $f_{120}$ . Freestream flow velocity of  $70 \text{ m s}^{-1}$ .

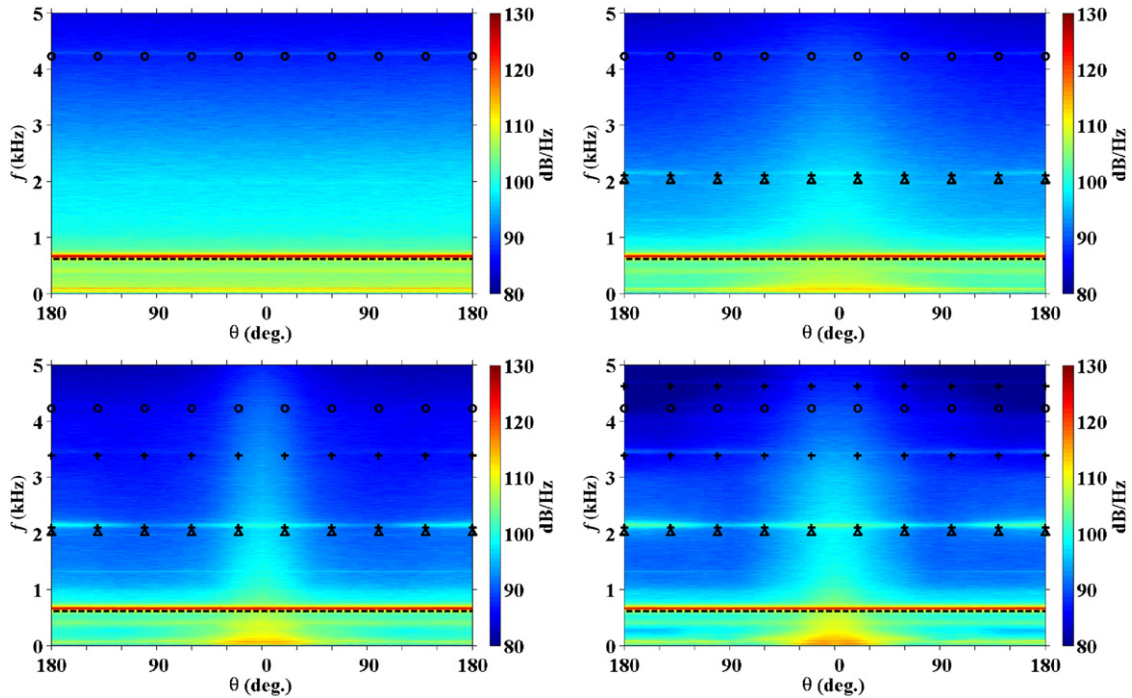


**Fig. 14.** Fluctuating wall-pressure spectra measured on the cavity floor at  $r=0, 12.5, 25, 37.5$  mm as a function of the polar angle  $\theta$ , where  $\theta=0^\circ$  designates the downstream direction. Acoustic cavity mode frequencies are represented by  $- - -$  for  $f_{100}$ ,  $\circ$  for  $f_{101}$ , and  $+$  for  $f_{110}, f_{120}$  and  $f_{130}$ . Freestream flow velocity of  $70 \text{ m s}^{-1}$ .

On the cavity floor, both azimuthal and radial modes are observed. This is visible in Fig. 14(a)–(d), which represent wall pressure spectra as a function of  $\theta$  on the cavity floor, respectively, for  $r=0, 12.5, 25$  and  $37.5$  mm. Fig. 14(a) is symmetrical by construction and included for comparison, showing the spectrum measured for  $r=0$  duplicated in the  $\theta$  direction. The  $\circ$  symbol corresponds to the first radial mode combined with the first depth mode,  $f_{101}$ . The observed pressure amplitude for this mode is maximum for  $r=0$  mm, which agrees with the Bessel function  $J_0$  function being maximal in zero. The azimuthal modes are again represented with  $+$  signals. The observed maximum amplitude of the first mode is at the microphone location farthest away from the centre, at  $r=37.5$ , while its predicted maximum is given by the maximum of  $J_1(\lambda_{01}r)$ , reached at  $r=r_0$ . All of the observed azimuthal modes have a maximum in  $\theta=0$ , i.e. for  $\psi=0$ . Their position is fixed by the recirculation at the downstream wall. At all depths on the cylindrical wall, a hump is present at around 3 kHz, which is too wide to be attributed to a specific cavity mode, and whose origin is not clear. Again at all depths, a very low frequency component,  $0 < f < 200$  Hz, is visible around  $\theta = \pm 120^\circ$ . This noise appears to be the trace of the upstream recirculation, which splits into a Y-shape before reaching the cavity mouth rather than follow directly the upstream edge at  $\theta = 180^\circ$ .

The fluctuating pressure signals discussed above were recorded simultaneously, and they can thus be studied with tools such as coherence and correlation functions. The coherence function  $\gamma^2$  between two signals  $u$  and  $v$  is defined as follows:

$$\gamma^2(f) = \frac{S_{uv} S_{uv}^*}{S_{uu} S_{vv}} \quad (2)$$

where  $S_{uv}$  is the cross-power spectral density function and  $*$  denotes the complex conjugate. This function is plotted in Fig. 15 for the upstream and downstream fluctuating wall pressure inside the cavity with an upstream flow velocity of  $70 \text{ m s}^{-1}$ .

An almost perfect coherence is obtained for the peak acoustic frequency of  $f=656$  Hz at both  $z=-0.1h$  and  $z=-0.75h$ , indicating as expected a strong acoustic correlation across the diameter of the cavity. There is also a significant peak in the coherence for  $f=400$  Hz, which is also visible in the shear layer impact zone in Fig. 13. This frequency is not noticeable in the far acoustic field, but nevertheless appears to be the continuation of the lower frequency mode referred to as mode 1 in Fig. 5(a). Acoustic cavity modes described previously are also clearly visible around  $f=2130$  Hz,  $f=3400$  Hz and  $f=4650$  Hz.

The time delay between the downstream and upstream fluctuating wall pressure signals can be estimated by computing the cross-correlation function  $R_{pp}(\tau)$

$$R_{pp}(\mathbf{x}_1, \mathbf{x}_2, \tau) = \frac{\overline{p'(\mathbf{x}_1, t + \tau) p'(\mathbf{x}_2, t)}}{\sqrt{\overline{p'^2(\mathbf{x}_1, t)}} \sqrt{\overline{p'^2(\mathbf{x}_2, t)}}} \quad (3)$$

between the two signals recorded at  $\mathbf{x}_1 = (r_0, 0, -0.1h)$  and  $\mathbf{x}_2 = (-r_0, 0, -0.1h)$ . This function is displayed in Fig. 16. Although the pressure signal inside the cavity is highly periodic, as can be seen from the strongly emerging single peak in

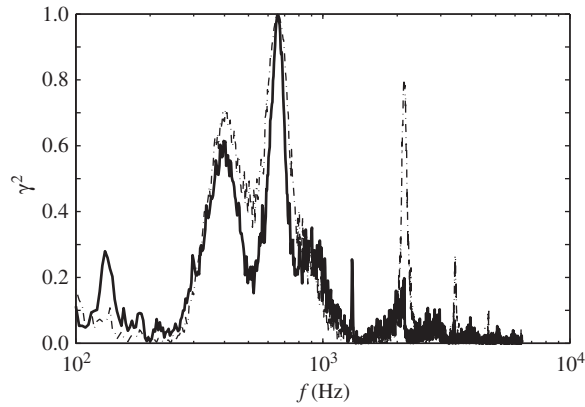


**Fig. 15.** Magnitude squared coherence, see expression (2), between downstream  $x=r_0$ , and upstream  $x=-r_0$ , fluctuating wall pressure for two microphone depths: —,  $z=-0.1$  h; - - -,  $z=-0.75$  h. Freestream flow velocity of  $70 \text{ m s}^{-1}$ .

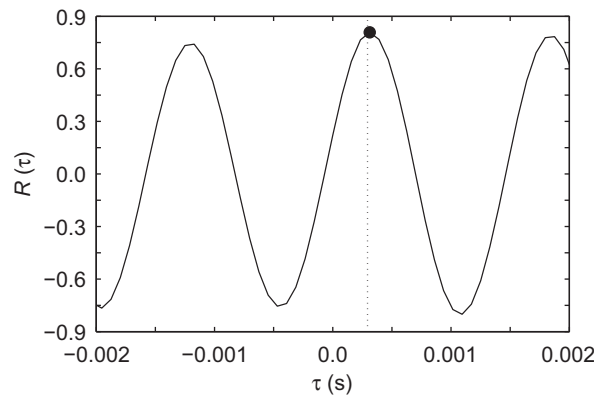


**Fig. 16.** Normalised cross-correlation function  $R_{pp}(\tau)$ , defined by relation (3), between downstream and upstream wall pressure, measured at  $\mathbf{x}_1 = (r_0, 0, -0.1 \text{ h})$  and  $\mathbf{x}_2 = (-r_0, 0, -0.1 \text{ h})$ , respectively. The maximum correlation is marked by the symbol • and the dashed line corresponds to the estimated acoustic propagation time  $\tau_a$ .

the spectra presented in Fig. 13, the correlation function exhibits a maximum for a time delay of  $\Delta\tau = 3.1 \times 10^{-4} \text{ s}$ . This time delay can be compared to the acoustic propagation time  $\tau_a$  across the cavity diameter  $d_0$  at an estimated velocity  $\bar{c}$  in the range  $c-U_\infty \leq \bar{c} \leq c$ , which yields  $3 \times 10^{-4} \leq \tau_a = D/\bar{c} \leq 4 \times 10^{-4} \text{ s}$ .

### 3.6.2. $U_\infty = 90 \text{ m s}^{-1}$ flow speed

The configuration at  $90 \text{ m s}^{-1}$  is interesting because it exhibits two nonharmonic peaks of similar amplitude in the acoustic far field, one at 500 Hz and the second at 794 Hz, as shown in Fig. 4(b). These frequencies coexist, as can be seen from the short-time Fourier transforms shown in Fig. 17(a) and (b), (a) corresponding to a 40 s period and (b) to a 2 s period of signal examined with 1024 points per FFT and 90 percent overlap between adjacent segments. While the lower frequency peak is more distinct and regular, there is no visible switching occurring between the two frequencies, and indeed both frequencies are simultaneously present for a large fraction of the time. The two peaks are therefore not the result of a mode-switching phenomenon observed in certain rectangular cavity flows [19,49].

Wall pressure measurements have also been performed at this flow speed. Fig. 18 shows the pressure spectra on the cavity walls, while spectra on the cavity floor are provided in Fig. 19. The two far-field peaks are visible at all locations on the wall and floor. Both the lower frequency peak at 500 Hz and the higher frequency peak at 794 Hz emerge considerably more strongly from background noise inside the cavity than in the far acoustic field, the difference being of around 6 dB. In addition to this, azimuthal modes are visible everywhere other than at  $r=0$  on the floor, and on the cavity floor the first radial mode is also present, as in the  $70 \text{ m s}^{-1}$  case. Both azimuthal and radial modes emerge from the background noise more strongly at  $90 \text{ m s}^{-1}$  than at  $70 \text{ m s}^{-1}$ . As in the  $70 \text{ m s}^{-1}$  configuration, a hump of undetermined origin is visible in the wall pressure spectra around  $f=3 \text{ kHz}$ . It is more intense than at the lower flow velocity, and appears to be stronger in the upstream direction around  $\theta = \pm 180^\circ$  than in the downstream direction. The low frequency trace of the Y-shaped recirculation is again visible around  $\theta = \pm 120^\circ$ .

The coherence function is plotted in Fig. 20 for the upstream and downstream fluctuating wall-pressure inside the cavity with an upstream flow velocity of  $90 \text{ m s}^{-1}$ . At this flow speed, a high level of coherence is obtained for the two

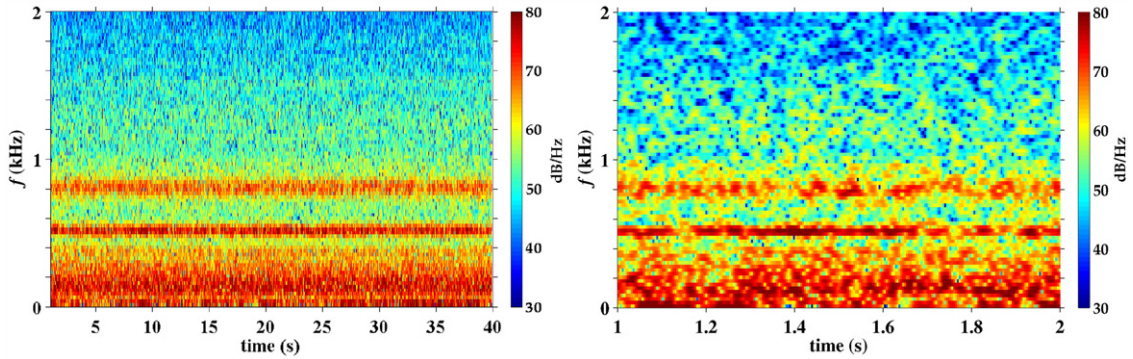


**Fig. 17.** Short-time Fourier transforms of the acoustic signal measured at  $z=1$  m above the cavity. FFTs computed with 1024 points, at a sampling frequency of 25 kHz, and an overlap of 90 percent. Freestream flow velocity of  $90 \text{ m s}^{-1}$ .

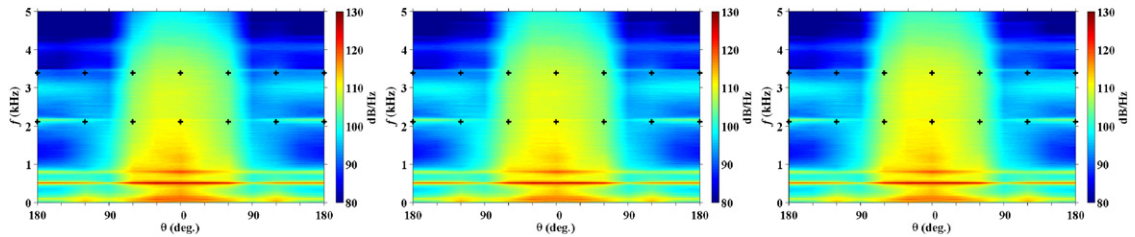


**Fig. 18.** Fluctuating wall-pressure spectra measured at  $z = -0.1, -0.5,$  and  $-0.75$  h along the circumference inside the cavity as a function of the polar angle  $\theta$ , where  $\theta = 0^\circ$  designates the downstream direction. Acoustic cavity modes  $f_{110}$  and  $f_{120}$  are represented by + symbols. Freestream flow velocity of  $90 \text{ m s}^{-1}$ .

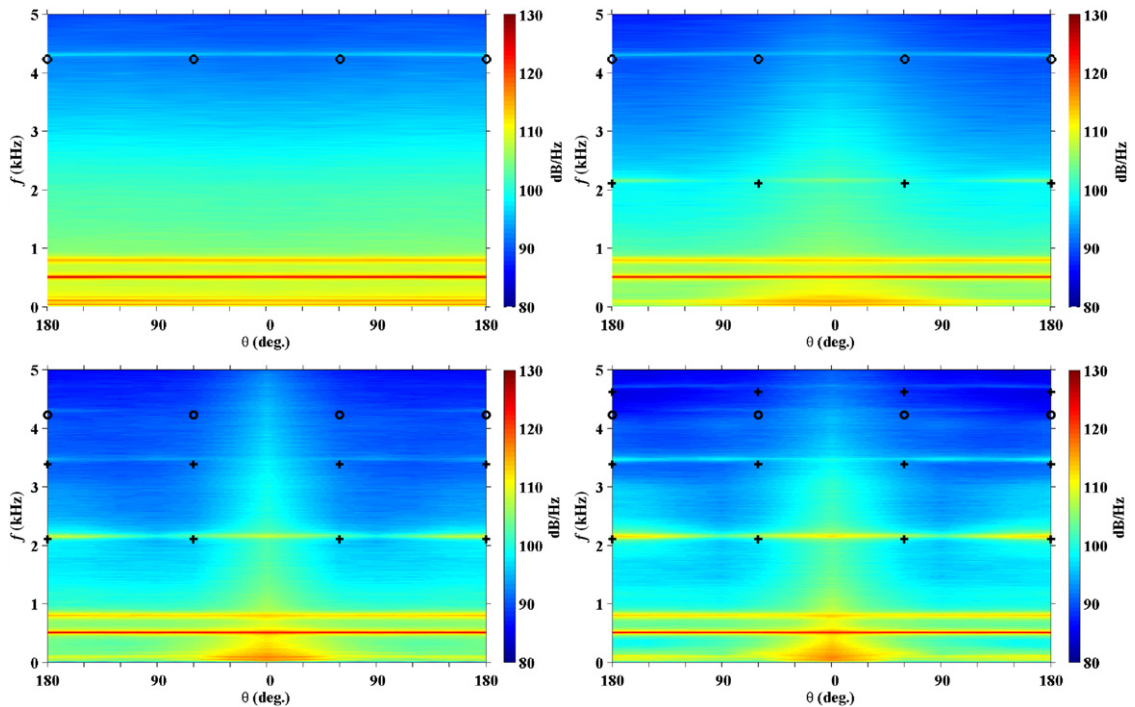


**Fig. 19.** Fluctuating wall-pressure spectra measured on the cavity floor at  $r=0, 12.5, 25, 37.5$  mm as a function of the polar angle  $\theta$ , where  $\theta = 0^\circ$  designates the downstream direction. Acoustic cavity modes are indicated by  $\circ$  for  $f_{101}$  and  $+$  for  $f_{110}, f_{120}$  and  $f_{130}$ . Freestream flow velocity of  $90 \text{ m s}^{-1}$ .

frequencies visible in the acoustic far field, at  $f=505$  Hz and  $f=800$  Hz, for both microphone depths  $z = -0.1h$  and  $z = -0.75h$ . The low frequency peak is around 8 dB more intense than the higher frequency peak in the far field, and its coherence is greater than 99 percent, as compared to 86 percent for the higher frequency. Acoustic modes in the cavity are again visible, with as expected higher levels of coherence than at  $70 \text{ m s}^{-1}$ .

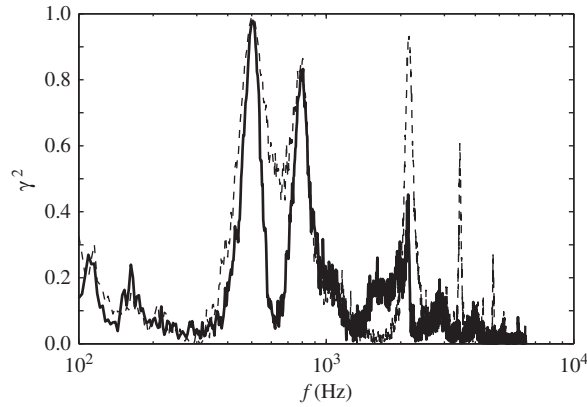


**Fig. 20.** Magnitude squared coherence, see expression (2), between downstream  $x=r_0$ , and upstream  $x=-r_0$ , fluctuating wall-pressure for two microphone depths: —,  $z=-0.1$  h; - - -,  $z=-0.75$  h. Freestream flow velocity of  $90 \text{ m s}^{-1}$ .

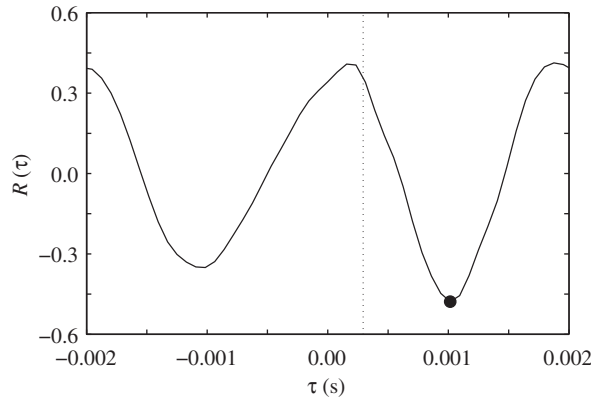


**Fig. 21.** Normalised cross-correlation function  $R_{pp}(\tau)$ , defined by relation (3), between downstream and upstream wall pressure,  $\mathbf{x}_1 = (r_0, 0, -0.1 \text{ h})$  and  $\mathbf{x}_2 = (-r_0, 0, -0.1 \text{ h})$ , respectively. The maximum correlation is marked by the symbol • and the dashed line corresponds to the estimated acoustic propagation time  $\tau_a$ .

The cross-correlation function  $R_{pp}(\tau)$  is again computed for the pressure signals recorded at  $\mathbf{x}_1 = (r_0, 0, -0.1 \text{ h})$  and  $\mathbf{x}_2 = (-r_0, 0, -0.1 \text{ h})$ , and shown in Fig. 21. Interestingly, the maximum correlation is found for a substantially larger time delay of  $\Delta\tau = 0.001 \text{ s}$ , as compared to  $3.1 \times 10^{-4}$  for the freestream velocity of  $U_\infty = 70 \text{ m s}^{-1}$ , and its value is negative.

#### 4. Nonlinear describing function model for cylindrical cavity noise

##### 4.1. Organised oscillations in cylindrical cavities

Fig. 5 exhibits similar trends to those measured in many studies on rectangular cavities [13,50,51]. A number of past experimental studies have shown that for rectangular cavities of aspect ratio  $L/H > 1$ , if strong acoustic fluctuations are produced, they are majoritarily due to synchronised shear layer fluctuations often referred to as Rossiter modes. As mentioned in the introduction, Rossiter [11] was the first to propose a physical explanation for such tonal noise generation in cavity flows, as well as a semi-empirical relationship predicting discrete Strouhal numbers at which such tones can be observed. Rossiter reasoned that tonal amplification was due to a feedback mechanism between vorticity creation at the cavity leading edge, and the noise emitted by the same vorticity impinging the downstream cavity wall after having been convected across the shear layer. His relationship (1) suggests that tonal amplification can take place at frequencies such that the convection time  $L/U_c$  for vortices across the cavity opening, added to the acoustic propagation time between the downstream and upstream cavity corners,  $L/c_\infty$ , is a multiple of the period, with the integer  $n$  corresponding to the average number of vortices in the shear layer.

This relationship has been shown to work well for a wide variety of different rectangular cavity configurations [5,6]. For round cavities, however, it does not seem well suited, since the Strouhal number relationship relies on convection and propagation times across the cavity opening being independent of the cross-flow  $y$  coordinate. This is obviously not the case for round cavities. Moreover, a strong dependence of the modes' frequencies on cavity depth is observed in

Fig. 5(a)–(c). While variants of Rossiter's formula such as that of Block [14] have been proposed to take into account depth effects for rectangular cavities, they do not correctly describe the variations observed in this work.

#### 4.2. Elder's model for cylindrical cavity noise

Elder [32] investigated depth-mode resonance of flush mounted cylindrical cavities in turbulent flows and developed a model for explaining and predicting their tonal behaviour. The model is based on the assumptions that the shear layer development is forced by the acoustic depth mode standing wave formed inside the cavity, and that the fluctuating mass flow into and out of the cavity generated by the shear layer is responsible for maintaining the standing wave's amplitude, as described in detail for the case of organ pipes [26]. Both the shear layer's effect on the acoustic standing wave and the acoustic effect on the shear layer are described by frequency response functions, whose product, for frequencies at which acoustic radiation is observed, should be equal to one. This approach has since been referred to as describing function analysis by Mast and Pierce [52] who studied the response of resonators to grazing flow.

In Elder's original work, the resonant cavity had a cylindrical pipe shape, but was partially closed on its flow-facing side by a rectangular aperture. His model predicted not only values of possible frequencies as a function of slot length, but also the variation of acoustic sound pressure amplitudes of different modes with slot length, yielding a good qualitative agreement for both aspects with his experimental data. In this work, a similar approach is followed for the case of an open cylindrical cavity.

#### 4.3. Forward transfer function

The effect of the acoustic depth mode on the shear layer above the cavity is first considered. The fluctuating volume flow generated by the unsteady shear layer through the cavity mouth, or drive flow, is related to the acoustic standing mode amplitude by a Forward Transfer Function  $G_{12} = q_h/q_{ac}$  where  $q_h$  is the hydrodynamic driving volume flow, and  $q_{ac} = w_{ac}S$  the acoustic volume flow due to the acoustic velocity  $w_{ac}$  through the cavity opening of area  $S = \pi r_0^2$ .

The drive flow is generated by the time dependent vertical velocity field through the cavity opening,  $q_h = \int_S \rho w$ . This quantity is in turn is estimated from the time-dependent vertical displacement of the shear layer above the cavity. Here we focus on the vertical displacement, noted  $\xi$ , of fluid particles in the time-dependent emission line from the upstream cavity edge. In the analysis performed by Elder,  $\xi$  was modeled as a one dimensional function, depending only on the streamwise  $x$  coordinate and on time, thanks to linear stability theory. This simplification was justified by the presence of the rectangular aperture placed over Elder's cavity, which firstly allowed the shear layer development to be assumed independent of the cross-stream  $y$  coordinate, and secondly allowed the streamwise evolution of the mean shear layer to be assumed slow. In the present case of a cylindrical cavity with no aperture, both of these assumptions appear to be somewhat bold. Indeed, shear layer properties undoubtedly have a dependence on  $y$  due to the circular opening. Moreover, the shear layer development near the upstream wall is influenced by the strong recirculation inside the cavity, while at the downstream end it is affected by its impingement on the cavity wall, suggesting that a 1D model based on stability theory is overly simplistic for the present study.

However, despite the seemingly oversimplistic nature of this model for the complex geometry in this work, it is shown in what follows to provide a reasonable prediction of acoustic frequencies resulting from the interaction between the flow and the cavity. The development of a more realistic model, for example based on a global stability analysis, would require greater knowledge of the mean flow field in the cavity than easily obtainable experimentally, and might thus be point of interest in a numerical study based on Large Eddy Simulation.

For a harmonically oscillating flow state, the displacement can be written as  $\xi(x,t) = A \cos(\omega t + \phi) = \text{Re}(a \exp(i(\omega t + \phi)))$  where  $\omega = 2\pi f$  is the angular frequency of interest,  $x$  is the streamwise coordinate with respect to the cavity mouth's centre, and  $a$  a spatially varying amplitude. In what follows, the Re operator will be omitted for concision. This displacement can be decomposed as the sum of an acoustic term and a term due to the shear layer's intrinsic instability. The acoustic displacement term is due to the acoustic velocity  $w_{ac}$  at the cavity mouth, which is assumed to be spatially uniform. The resulting displacement can thus be written as  $(w_{ac}/i\omega)\exp(i\omega t)$ . The transverse wave term is modeled following Michalke's work on spatially evolving disturbances in a shear layer [53]. It is of a convective nature, and thus has an  $(\omega t - kx)$  dependence where the wavenumber  $k$  is a function of frequency  $f$ , freestream flow velocity  $U_\infty$  and an upstream length scale of the initial shear layer  $\delta_{\omega_0} = U_\infty/(2 dU/dz)$ . The wave's amplitude is assumed to grow exponentially in the streamwise direction, with a spatially varying growth rate  $\alpha$  computed from the local velocity profile. Given the simplistic nature of the modeling undertaken here, the displacement's dependence on  $z$  is neglected. These different points allow the instability displacement at location  $x$  to be written as

$$A \exp\left(\int_{-r_0}^x \alpha(x') dx'\right) \exp[i(\omega t - kx)]$$

where  $A$  is now a constant. Thus the total displacement  $\xi$  can be written

$$\xi(x,t) = (w_{ac}/i\omega)\exp(i\omega t) + A \exp\left(\int_{-r_0}^x \alpha(x') dx'\right) \exp[i(\omega t - kx)]$$

This previous expression can be simplified by noting the boundary condition which must be satisfied by  $\xi$  immediately downstream of the separation point,

$$\lim_{x \rightarrow -r_0} \xi(x, t) = 0$$

Accordingly, the constant  $A$  can be expressed in terms of acoustic displacement, yielding the following expression for total displacement:

$$\xi(x, t) = (w_{ac}/i\omega)\exp(i\omega t) \left\{ 1 - \exp\left(\int_{-r_0}^x \alpha(x') dx'\right) \exp(-ik(x+r_0)) \right\}$$

Fig. 22(a)–(d) illustrates the manner in which the hydrodynamic drive flow is estimated from the interface displacement. They show the position of the emission interface in the  $y=0$  plane at four equally spaced instants of a period for a shear layer dominated by a single large perturbation. Arrows represent the direction of fluid particles from the outer region, in white, and from the inner region, in black. The flow entering the cavity is maximum at instant (b), when the displacement streamwise profile is entirely inside the cavity. At this moment, for  $x < 0$  outside flow is entering the cavity, and over the second half of the cavity the flow near the interface is essentially horizontal. This instant is referred to as *closure* in Elder’s work. One half period later in the cycle, see Fig. 22(d), the displacement streamwise profile is located entirely outside the cavity, and because of the fluid particles exiting through the first half of the cavity  $x < 0$ , outgoing volume flow is at its maximum. Instants shown in Fig. 22(a) and (c) correspond roughly to moments in the cycle when outgoing flow is approximately balanced by entering flow, yielding an overall volume flow through the cavity opening close to zero.

The amplitude of the time-varying volume flow can be estimated from the positions of the interface at maximum inflow and outflow, shown, respectively, in Fig. 23(a) and (b). In these views,  $x_M$  marks the streamwise location at which the displacement at closure is maximum. This maximum displacement is noted  $\xi_M$ . At closure, the volume flow  $q_+$  passing between the  $z=0$  plane and the interface at  $x_M$ , whose velocity is noted  $u_+$  in Fig. 23(a), is roughly equal to the volume flow entering the cavity. Indeed, downstream of  $x_M$  the flow is essentially horizontal and therefore does not contribute to the volume flow. The volume inflow is thus located upstream of  $x_M$ , and by continuity is equal to  $q_+$ . A similar reasoning yields  $q_-$  as the maximum volume outflow, occurring half a period later and shown in Fig. 23(b). It should be noted at this point that this reasoning should be performed on the streamline leaving the cavity’s leading edge, rather than on the corresponding emission line, in order for the continuity argument to be fully valid. Here, it is assumed that the maximum displacement of the streamline at location  $x_M$  is equal to the maximum displacement of the emission line,  $\xi_M$ . The accuracy of this assumption will be assessed later based on experimental data. It is now necessary to estimate  $q_+$  and  $q_-$  to obtain the amplitude of the volume flow oscillations. For a rectangular cavity opening,  $q_+$  and  $q_-$  can be easily estimated as the product of the spatial-average flow velocity at streamwise position  $x_M$ , respectively,  $u_+$  and  $u_-$ , by the dimensions through which this flow is passing  $\xi_M W$  where  $W$  is the rectangular cavity’s width. The drive flow amplitude would then be given by  $q_h = W\xi_M(u_+ + u_-)/2$ , which, for moderate oscillation amplitudes, could be approximated by  $q_h = W\xi_M U_0$  where  $U_0$  is the time averaged velocity at  $x_M$  and  $z=0$ . For cylindrical cavities, the effective cross-stream width depends on the streamwise position  $x$  according to  $2\sqrt{r_0^2 - x^2}$ . Nevertheless, the same

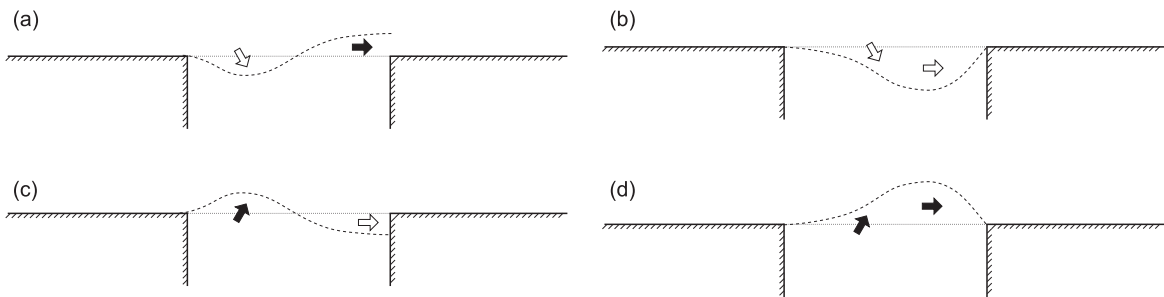


Fig. 22. Interface displacement over one period illustrated for the mode  $N=1$ , arrows indicate flow direction through the cavity mouth.

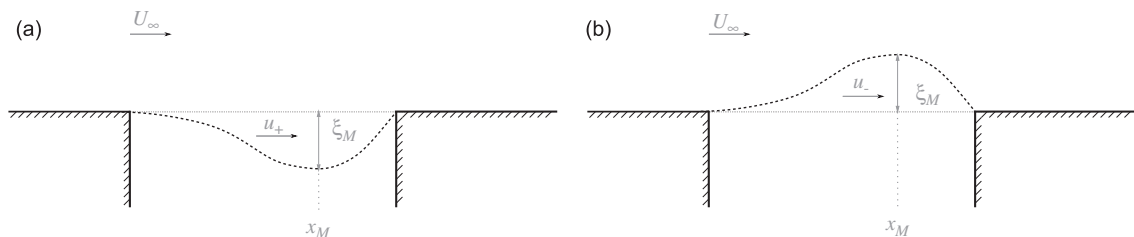


Fig. 23. Maximum inflow (a) and outflow (b) instants in a cycle.

method is used here to provide a rough approximation of the drive flow generated by the shear layer in the present cylindrical cavity configuration, explicitly  $q_h = 2\sqrt{r_0^2 - x_M^2} \xi_M U_0$ .

In order to use the above expression of the driving volume flow,  $x_M$  and  $\xi_M$  must be calculated. In Elder's work, amplification of the wave term along the shear layer was sufficiently small to be neglected, allowing the wave term to be simplified to  $-(w_{ac}/i\omega)\exp[i(\omega t - kx)]$ . At the same time, Elder observed that over the second half of the mouth opening, the acoustic contribution to total displacement  $\xi$  could also be neglected, with the waveform  $\xi = i(w_{ac}/\omega)\exp[i(\omega t - kx)]$  correctly describing his experimental data. In the study presented here, streamwise amplification of the wave term appears to be substantial, as will be shown subsequently. This suggests that the acoustic term can also be neglected for the cylindrical cavity, allowing the interface displacement over the second half of the cavity mouth to be written

$$\xi(x, t) = i(w_{ac}/\omega)\exp\left(\int_{-r_0}^x \alpha(x') dx'\right)\exp[i(\omega t - k(x + r_0))] \tag{4}$$

The maximum displacement position  $x_M$  corresponds to largest value of  $x$  verifying  $d\xi/dx = 0$  at closure. It is assumed that the streamwise amplification

$$\exp\left(\int_{-r_0}^x \alpha(x') dx'\right)$$

is sufficiently slow for the maximum of  $\xi(x)$  to be given by the maximum of  $\text{Re}(i \exp[i(\omega t - k(x + r_0))])$ , or in other words the values of  $x$  annulling  $d\xi/dx$  are approximately those annulling

$$d\{-(w_{ac}/\omega)\sin(\omega t - k(x + r_0))\}/dx$$

Accordingly,  $x_M$  verifies

$$\omega t_M - k(x_M + r_0) = -(2N - 1)\pi/2, \quad N = 1, 2, 3, \dots$$

where  $N$  corresponds to the average number of structures of wavelength  $\lambda$  along the shear layer. At closure, the displacement at the downstream corner is also zero, as shown in Fig. 22(b), providing the second condition

$$kD - \omega t_M = N\pi$$

These two relations combined yield the desired position  $x_M$  as  $x_M = r_0 - \lambda/4$ , which can be injected into Eq. (4) to provide

$$\xi_M(t) = i(w_{ac}/\omega)\exp\left(\int_{-r_0}^{x_M} \alpha(x') dx'\right)\exp[i(\omega t - k(D - \lambda/4))] = (w_{ac}/\omega)\exp\left(\int_{-r_0}^{x_M} \alpha(x') dx'\right)\exp[i(\omega t - kD + \pi)]$$

Finally, the forward transfer function  $G_{12}$  can be written as

$$G_{12} = \frac{q_h}{q_{ac}} = \frac{2\sqrt{r_0^2 - x_M^2} \xi_M U_0}{S w_{ac} \exp(i\omega t)} = A \exp[i(-kD + \pi)] \tag{5}$$

where

$$A = 2\sqrt{r_0 \lambda / 2 - \lambda^2} / 16 U_0 / (S \omega) \exp\left(\int_{-r_0}^{x_M} \alpha(x') dx'\right)$$

corresponds to an amplitude term.

#### 4.4. Backward transfer function

The Backward Transfer Function,  $G_{21} = q_{ac}/q_h$  describes the efficiency with which the deep cavity converts the drive flow  $q_h$  into the acoustic forcing term  $q_{ac}$ . It can be expressed using the acoustic impedance of the cavity as seen from the mouth,  $Z_C$ , and the impedance of the opening as seen from inside the cavity,  $Z_M$ .

The cavity impedance can be written analytically as  $Z_C = (\rho c/S)(\alpha_0 h - i \cot(k_0 h))$  where  $\alpha_0$  is the acoustic attenuation coefficient per unit length in a pipe and  $k_0 = \omega/c$  the acoustic wavenumber.

The mouth impedance  $Z_M$  is modeled as that of an infinitely flanged round pipe [48] in the linear regime and for a medium at rest. This impedance is written as  $Z_M \simeq (\rho c/S)(1 + R)/(1 - R)$ , and following the work of Norris and Sheng [54], the reflexion coefficient  $R = |R|\exp(2ik_0 \delta_h)$  is approximated thanks to its amplitude  $|R| \simeq 1 - 0.5(k_0 r_0)^2$  and the length correction  $\delta_h \simeq r_0(0.82159 - 0.49(k_0 r_0)^2)/(1 - 0.46(k_0 r_0)^3)$ . The influence of grazing flow on the termination impedance depends strongly on the ratio of diameter to boundary layer thickness. For small diameters, typically  $D/\delta_{99} < 0.5$ , numerous studies focused on acoustic liner behaviour have shown that resistance increases roughly linearly with grazing flow speed [55,56], while reactance varies in a less predictable fashion. For larger orifices also, impedance varies with grazing flow as a function of the diameter-based Strouhal number, as measured by Ronnenberger [57]. This variation is large for low Strouhal numbers  $St < 1.2$ , but for larger Strouhal numbers the impedance converges towards its value in the absence of grazing flow. Given the high minimum Strouhal number of oscillations observed in this work,  $St_{\min} = \omega D/U_\infty = 1.66$ , the cavity mouth impedance should not vary significantly from its value for a medium at rest. Unlike in Elder's work, in this study it

should not be necessary to specify a nonlinear resistance term proportional to  $|w_{ac}|/c$  in the mouth impedance, as the small depth-to-diameter ratio induces large linear resistance in the mouth:  $|w_{ac}|/c \ll 1/2(k_0r_0)^2$ . Using these terms, the Backwards Transfer Function is simply written

$$G_{21} = -Z_C/(Z_M + Z_C) \tag{6}$$

#### 4.5. Transfer function product

Given the definitions of  $G_{12}$  and  $G_{21}$  seen previously, configurations exhibiting stable harmonic acoustic radiation should verify the condition  $G_{12}G_{21} = 1$ . Elder used this condition to obtain oscillation parameters at resonance, i.e. at frequencies corresponding to a cavity depth mode, and to determine for what slot lengths  $H$  resonance would be achieved.

In this work, the approach is used to estimate the effect of flow velocity on acoustic frequencies emitted by a round cavity. This complex equality  $G_{12}G_{21} = 1$  has two parts, requiring both the modulus to be equal to 1 and the argument to be nil. The argument describes the necessary phase match between the forward and backward transfer functions, and thus provides possible feedback frequencies. In this respect it is similar to Rossiter’s formula for rectangular frequencies, in that it gives no indication as to which of these possible frequencies are indeed present in a given configuration. This role is performed by the modulus part of the equality. Frequencies present in the far acoustic field should verify  $|G_{12}G_{21}| = 1$ , while those such that  $|G_{12}G_{21}| < 1$  should be stable.

The argument of the transfer function product is evaluated for the geometry and flow speeds studied in this work. Parameters necessary for the forward transfer function, in particular  $U_0$ , are computed from the PIV data measured at  $70 \text{ m s}^{-1}$ , and scaled linearly with flow velocity. Depending on the flow velocity, one or two frequencies are found to verify the condition

$$\arg(G_{12} \times G_{21}) = 0 \tag{7}$$

As noted by Elder, these frequencies approximately verify the condition  $kD = 2N\pi - \pi/2$  where  $N = 1, 2, 3, \dots$  corresponds to the number of large-scale vortices in the shear layer. The two frequency modes obtained by solving Eq. (7) are represented in Fig. 5(a)–(c) by white circles. A good agreement is observed for both modes at all frequency depths. This strongly suggests that the dominant behaviour for these geometries is acoustic depth modes coupling with the two first shear layer modes. This can be regarded as a strong coupling, in the sense that observed frequencies are not simply fixed by the depth mode, as has been observed for substantially deeper cavities, but are instead velocity-dependent equilibria between losses due to acoustic radiation and gains due to shear layer dynamics.

The modulus of the transfer function product computed from the model is too large, with  $|G_{12}G_{21}| \geq 2.5$  for frequencies at which tones are observed in the far field, indicating that the amplitude of the forward transfer function  $G_{12}$  is likely overestimated due to the assumptions made in its derivation. This overestimation is discussed in Section 4.6.

#### 4.6. Comparison with high-speed PIV data

High-speed PIV data was obtained in the  $y=0$  plane of the shear layer for the freestream flow velocity of  $70 \text{ m s}^{-1}$ . This data allows different aspects of the previously presented model to be examined in more detail.

In order to illustrate the importance of shear layer amplification in this work, approximate interface waves are shown at four equally spaced times in the acoustic period in Fig. 25 for a freestream flow velocity of  $70 \text{ m s}^{-1}$ . These interface waves have been inferred from high-speed shear layer PIV images as follows. The PIV flow fields are sorted and phase-averaged thanks to a pressure signal recorded at the bottom of the cavity, which is synchronised with the PIV system. The pressure signal is mostly harmonic, but it exhibits periods during which the main frequency is drowned out by other flow features. Only images corresponding to relatively sinusoidal portions of the pressure signal are retained for the phase averaging. In practice about two thirds of the signal was rejected based on this criterion. The remaining flow fields were separated into twelve time intervals or bins, and each bin was averaged according to the technique proposed by Hussain and Reynolds [58] to obtain the ensemble averaged and cyclic horizontal and vertical components of the shear layer flow,  $U, W, \tilde{u}$  and  $\tilde{w}$ . The cyclic fields  $\tilde{u}(x,z,t)$  and  $\tilde{w}(x,z,t)$  were then each fitted by a function  $a(x,z)\sin(\omega t - \phi(x,z))$ , in which both the spatial amplitude  $a$  and the phase  $\phi$  were low-pass filtered. The resulting filtered fields provided a reasonable match with the initial data, the r.m.s. difference between the PIV data and the filtered fields not exceeding 30 percent throughout the shear layer. Fig. 24(a) and (b) provides an illustration of this fit, showing

$$\sqrt{\int_0^T [a \sin(\omega t - \phi) - \tilde{w}(t)]^2 dt} / \max(\tilde{w})$$

in the shear layer and  $a \sin(\omega t - \phi)$  and  $\tilde{w}$  at  $(x = r_0/2, z = 0)$  over one period  $T$ , respectively. The high levels of relative error observed outside the shear layer in Fig. 24(a) reflect the low value of  $\max(\tilde{w})$  in these zones. This procedure allowed for  $\tilde{u}$  and  $\tilde{w}$  to be inferred at any time in the acoustic cycle. The phase-averaged fields thus obtained were used to compute time dependent particle emission lines from the upstream cavity edge, by integrating  $U + \tilde{u}(x,z,t)$  and  $W + \tilde{w}(x,z,t)$ . These

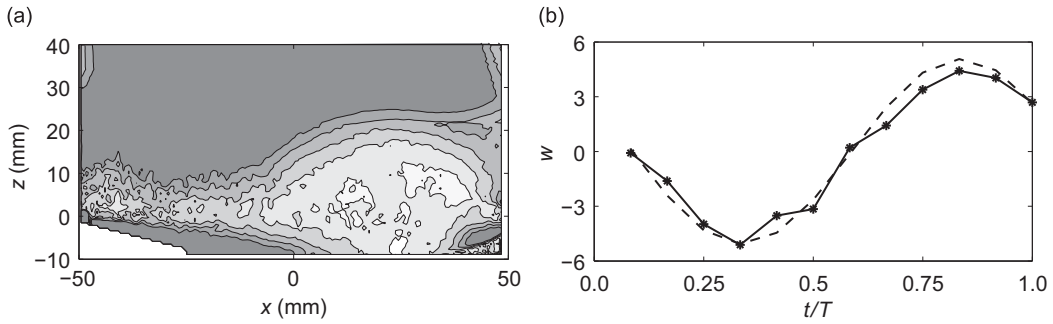


**Fig. 24.** Match between PIV data  $\tilde{w}$  and fitted sinusoidal velocity  $a \sin(\omega t - \phi)$ . RMS differences in the shear layer (a), with contours ranging from 10 percent to 50 percent of local velocity amplitude  $\max(\tilde{w})$ , and  $\tilde{w}$  ( $-\bullet-\bullet-$ ) and  $a \sin(\omega t - \phi)$  at  $(x = r_0/2, z = 0)$  ( $- - -$ ) over one period (b).

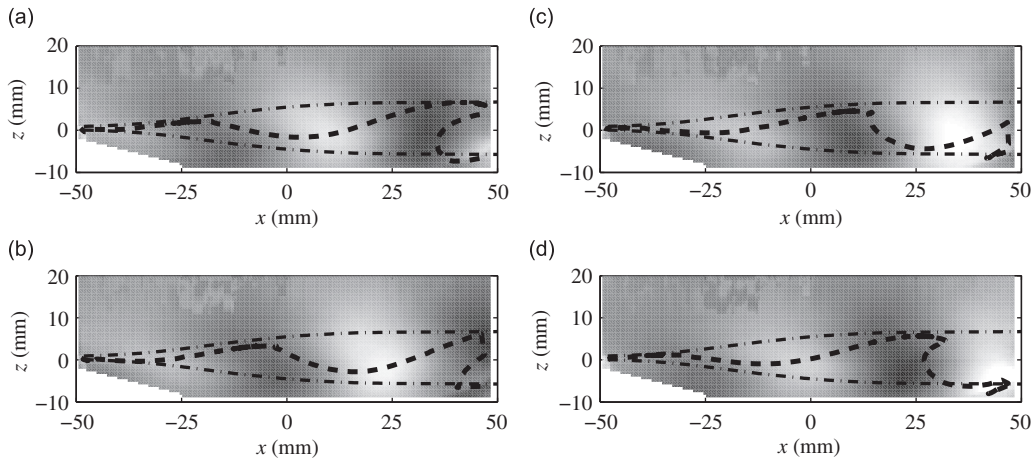


**Fig. 25.** Interface (dashed line) and cyclic vertical velocity perturbations during one acoustic cycle, estimated from high-speed PIV. Grey scale ranges from  $-6$  (white) to  $6$  (black)  $\text{m s}^{-1}$ . The perturbation envelope predicted by linear stability theory is represented as dashed-dotted lines.

particle positions are represented by dashed lines in Fig. 25. Also represented is the envelope given by the instability amplification

$$\exp\left(\int_{-r_0}^{x_M} \alpha(x') dx'\right)$$

multiplied by the acoustic displacement amplitude  $w_{ac}/\omega$ , shown in dashed-dotted lines. The acoustic velocity  $w_{ac}$  is estimated from the pressure signal at the bottom of the cavity, at around  $2.5 \text{ m s}^{-1}$ . Unlike in Elder’s study, interface displacement clearly grows as perturbations are convected along the shear layer, and the maximum displacement is roughly ten times greater than the acoustic displacement. It can be seen from Fig. 25 that the maximum displacement obtained from PIV is in fact reasonably well predicted by linear stability theory.

Another point that can be examined from the PIV is that of the estimation of the drive flow  $q_h$  according to  $q_h = 2\sqrt{r_0^2 - x_M^2} \xi_M U_0$ . The PIV flow data allows  $\xi_M$  to be estimated at around  $6 \text{ mm}$  according to the technique described previously, and  $U_0 = 25 \text{ m s}^{-1}$ . The driving volume flow would thus be  $q_h \approx 1.3 \times 10^{-2} \cos(\omega t) \text{ m}^3 \text{ s}^{-1}$ . The volume flow thus estimated relies on the assumption that the maximum streamline deviation at  $x_M$  is equal to the maximum emission line deviation at the same location,  $\xi_M$ . Upon verification with the fitted data,  $\xi_M$  is approximately 2.2 times the streamline displacement, leading to a revised estimation of the volume flow, by this method, of  $q_h \approx 6 \times 10^{-3} \cos(\omega t) \text{ m}^3 \text{ s}^{-1}$ . The phase-averaged cyclic velocity fluctuation  $\tilde{w}(x, z, t)$  can also be used directly to obtain an estimation of  $q_h$  according to

$$q_h(t) = \int_{-r_0}^{r_0} 2\sqrt{r_0^2 - x^2} \tilde{w}(x, z = 0, t) dx$$

which yields  $q_h(t) \approx 4 \times 10^{-3} \cos(\omega t) \text{ m}^3 \text{ s}^{-1}$ . Both of these estimations are based on the assumption that important flow quantities,  $\xi_M$  and  $U_0$  for the first method and  $\tilde{w}$  for the second, are uniform across the cavity opening in the cross-stream  $y$  direction.

Nevertheless, with the second estimation obtained by integrating  $\tilde{w}(x, z = 0, t)$  for  $70 \text{ m s}^{-1}$ , the product  $G_{12}G_{21}$  has a value of 1.1, close to the expected value of 1. Thus this approach successfully predicts frequencies at which oscillations can be

observed for the configurations studied in this work, but due to considerable uncertainty in the determination of the forward transfer function's magnitude, prediction of the acoustic amplitude reached for these frequencies cannot be expected.

#### 4.7. Interpretation of acoustic data

Results presented in Section 3.1 are now discussed in light of the model proposed in this work.

Parthasarathy et al. [33] studied the acoustic radiation of small deep round cavities under grazing flow, and proposed a simple 1D forced oscillator analogy explaining the effect of the grazing flow on the frequency of a round cavity's acoustic resonance, as a comparison to his experimental data. The conclusion of his study was that for low Mach number grazing flows,  $M < 0.2$ , and relatively deep cavities, typically  $D/h < 0.5$ , acoustic wavelength  $\lambda$  is roughly proportional to both the effective depth [59,60] ( $h + \alpha D$ ) with  $\alpha = 1$ , and to the factor  $(1 - M)$ . He found that the simple empirical formula  $\lambda/(h + D) = 4(1 - M)$  described his data well. Parthasarathy referred to such behaviour as acoustic resonance, as opposed to shear layer resonance. Although Parthasarathy's simple formula matches some of the frequencies observed to a reasonable extent, the overall match is less good than that given by Elder's model, given in expression (7), and is accordingly not shown here. Parthasarathy also examined the acoustic SPL emitted by a round cavity as a function of velocity, and found that radiated pressure increased linearly with velocity, i.e.  $\text{SPL} = \text{SPL}_{\text{ref}} + 20 \log_{10}(U_{\infty}/U_{\text{ref}})$ . This is clearly not the case with the current results, as can be seen in Fig. 4.

The adaptation of Elder's model to the cylindrical cavity provides acoustic frequencies that match those observed in experimental data, and its description of shear layer behaviour also compares favourably to that deduced from high speed PIV results at a freestream flow velocity of  $70 \text{ m s}^{-1}$ . The cavity's general dynamics can therefore reasonably be interpreted according the model's assumption of coupling between large scale shear layer fluctuations and the cavity's acoustic depth mode. Both the decrease in frequencies and the rise in sound level as cavity depth is increased, reported in Section 3.1 and Fig. 5(a)–(c), are consistent with the cavity's depth mode playing an active part in noise generation.

The higher frequency mode labeled (2) in Fig. 5 is generated by an average of two large structures in the shear layer, while the lower frequency mode (1) results from a single large structure. The higher frequency mode (2) dominates for flow velocities between  $50$  and  $80 \text{ m s}^{-1}$  for the cavity of depth  $100 \text{ mm}$ , while the lower frequency mode (1) is the main contributor to far field sound levels for flow velocities above  $100 \text{ m s}^{-1}$ . Wall pressure measurements inside the cavity for a flow speed of  $70 \text{ m s}^{-1}$ , described in Section 3.6.1, show the presence of a low frequency that corresponds to the continuation of mode (1), despite this mode not being visible in the far field. For flow speeds in the range of  $80$ – $100 \text{ m s}^{-1}$ , the model suggests that both shear layer modes (1) and (2) are active and of comparable magnitude. Wall pressure results discussed in Section 3.6.2 show that the frequencies associated with the two modes coexist rather than compete. Future experiments or computations might allow to confirm and study more in detail the simultaneous presence of two large structures of different wavelengths in the shear layer. The presence of two coherent structures associated with the second shear layer mode is confirmed by two-point velocity correlations described in Section 3.5 as well as phase-averaged velocity fields discussed in Section 4.6.

## 5. Conclusions

Acoustic radiation and flow characteristics around a circular cylindrical  $10 \text{ cm}$ -diameter cavity under grazing flow have been studied experimentally. Flow features have been studied thanks to HWA, LDA and PIV techniques, and inner cavity fluctuating pressure measured with wall-mounted microphones. Cavity depths from  $100$  to  $150 \text{ mm}$  have been studied, at flow velocities between  $50$  and  $110 \text{ m s}^{-1}$ .

For the  $100 \text{ mm}$  deep cavity, far-field acoustic power is shown to vary roughly with the sixth power of the upstream Mach number over the range of flow velocities studied. Strong depth- and velocity-dependent tonal components are observed in the far acoustic field at all flow velocities. These discrete frequencies are well described by a shear-layer excitation of the cavity's acoustic depth mode. Depending on the freestream flow velocity, one or two modes are simultaneously present. The shear layer impact on the downstream cavity edge also excites other cavity modes. Both radial and azimuthal modes are observed, and their intensity is observed to increase with flow velocity and cavity depth.

A feedback model based on the interaction of the cavity's acoustic depth mode with large scale shear layer fluctuations is proposed. The model uses linear stability theory to describe shear layer behaviour over the cavity opening, and classical acoustic results to model the cavity's response to shear layer forcing. Acoustic tones measured in the far field are well matched by the model's predictions.

## Acknowledgments

Christophe Bailly is also a member of the Institut Universitaire de France. Parts of this work were supported by the Fondation de Recherche pour l'Aéronautique & l'Espace (FRAE) under contract reference AFB AEROCV. The authors wish to thank Damien Desvigne for interesting discussions regarding the model developed in this work. The authors further acknowledge discussions with Dr. Alois Sengissen (Airbus-France).

## References

- [1] J. Huber, S. Illa, Jet noise assessment and sensitivity at aircraft level, *Thirteenth AIAA/CEAS Aeroacoustics Conference*, AIAA Paper 2007-3728, 2007.
- [2] M. Czech, J. Crouch, R. Stoker, Cavity noise generation for circular and rectangular vent holes, *Twelfth AIAA/CEAS Aeroacoustics Conference*, AIAA Paper 2006-2508, 2006.
- [3] A. Roshko, Some Measurements of Flow in a Rectangular Cutout, Technical Note 3488, NACA, 1955.
- [4] Krishnamurty Karamcheti, Acoustic Radiation from Two-dimensional Rectangular Cutouts in Aerodynamic Surfaces, Technical Note 3487, NACA, 1955.
- [5] D. Rockwell, E. Naudascher, Review—self-sustaining oscillations of flow past cavities, *ASME Journal of Fluids Engineering* 100 (1978) 152–165.
- [6] D. Rockwell, Oscillations of impinging shear layers, *AIAA Journal* 21 (5) (1983) 645–664.
- [7] C. Tam, P. Block, On the tones and pressure oscillations induced by flow over rectangular cavities, *Journal of Fluid Mechanics* 89 (2) (1978) 373–399.
- [8] K. Ahuja, J. Mendoza, Effects of Cavity Dimensions, Boundary Layer, and Temperature in Cavity Noise with Emphasis on Benchmark Data to Validate Computational Aeroacoustic Codes, NASA CR-4653, 1996.
- [9] M. Gharib, A. Roshko, The effect of flow oscillations on cavity drag, *Journal of Fluid Mechanics* 177 (2003) 501–530.
- [10] S. Grace, W. Dewar, D. Wroblewski, Experimental investigation of the flow characteristics within a shallow wall cavity for both laminar and turbulent upstream boundary layers, *Experiments in Fluids* 36 (2004) 791–804.
- [11] J. Rossiter, Wind-tunnel Experiments on the Flow Over Rectangular Cavities at Subsonic and Transonic Speeds, Technical Report 3438, Aeronautical Research Council Reports and Memoranda, 1964.
- [12] A. Powell, On the edgetone, *Journal of the Acoustical Society of America* 33 (4) (1961) 395–409.
- [13] H. Heller, D. Holmes, E. Covert, Flow-induced pressure oscillations in shallow cavities, *Journal of Sound and Vibration* 18 (1971) 545–553.
- [14] P.J.W. Block, Noise Response of Cavities of Varying Dimensions at Subsonic Speeds, NASA Technical Note D-8351, 1976.
- [15] A. Bilanin, E. Covert, Estimation of possible excitation frequencies for shallow rectangular cavities, *AIAA Journal* 11 (1973) 347–351.
- [16] W. Blake, Mechanics of flow-induced sound and vibration, *General Concepts and Elementary Sources*, vol. 1, Academic Press, Inc, 1986, pp. 130–149 (Chapter 3).
- [17] C. Rowley, T. Colonius, A. Basu, On self-sustained oscillations in two-dimensional compressible flow over rectangular cavities, *Journal of Fluid Mechanics* 455 (2002) 315–346.
- [18] X. Gloerfelt, C. Bailly, D. Juvé, Direct computation of the noise radiated by a subsonic cavity flow and application of integral methods, *Journal of Sound and Vibration* 266 (1) (2003) 119–146.
- [19] X. Gloerfelt, C. Bogey, C. Bailly, Numerical evidence of mode switching in the flow-induced oscillations by a cavity, *International Journal of Aeroacoustics* 2 (2) (2003) 193–217.
- [20] L. Larchevêque, P. Sagaut, T.-H. Lê, P. Comte, Large-eddy simulation of a compressible flow in a three-dimensional open cavity at high Reynolds number, *Journal of Fluid Mechanics* 516 (2004) 265–301.
- [21] D.P. Rizzetta, M.R. Visbal, Large-Eddy Simulation of supersonic cavity flowfields including flow control, *AIAA Journal* 41 (8) (2003) 1452–1462.
- [22] O. Marsden, X. Gloerfelt, C. Bailly, Direct noise computation of adaptive control applied to a cavity flow, *Comptes Rendus à l'Académie des Sciences* 331 (2003) 423–429.
- [23] L. Cattafesta, D. Williams, C. Rowley, F. Alvi, Review of active control of flow-induced cavity resonance, *Thirty-third AIAA Fluid Dynamics Conference*, Orlando, FL, June 2003.
- [24] C. Rowley, D. Williams, Dynamics and control of high-Reynolds-number flow over open cavities, *Annual Review of Fluid Mechanics* 38 (2006) 251–276.
- [25] L. Cremer, H. Ising, Die selbsterregte schwingungen von orgelpfeifen (The self-induced vibrations of organ pipes), *Acústica* 19 (1967) 143–153. (in German).
- [26] S. Elder, On the mechanisms of sound production in organ pipes, *Journal of the Acoustical Society of America* 54 (6) (1973) 1554–1564.
- [27] M. Howe, The dissipation of sound at an edge, *Journal of Sound and Vibration* 70 (3) (1980) 407–411.
- [28] J. Bruggeman, Flow-induced Pulsations in Pipe Systems, PhD Thesis, Eindhoven University of Technology, 1987.
- [29] S. Ziada, S. Shine, Strouhal numbers of flow-excited acoustic resonance of closed side branches, *Journal of Fluids and Structures* 13 (1) (1999) 127–142. <http://dx.doi.org/10.1006/jfls.1998.0189>.
- [30] U. Ingard, V. Singhal, Flow excitation and coupling of acoustic modes of a side-branch gravity in a duct, *Journal of the Acoustical Society of America* 60 (5) (1976).
- [31] W. Jungowski, K. Botros, W. Studzinski, Cylindrical side-branch as tone generator, *Journal of Sound and Vibration* 131 (2) (1989) 265–285.
- [32] S. Elder, Self-excited depth-mode resonance for a wall-mounted cavity in turbulent flow, *Journal of the Acoustical Society of America* 64 (3) (1978) 877–890.
- [33] S. Parthasarathy, Y. Cho, L. Back, Sound generation by flow over relatively deep cylindrical cavities, *Journal of the Acoustical Society of America* 78 (5) (1985) 1785–1795.
- [34] O. Marsden, E. Jondeau, P. Souchotte, C. Bailly, C. Bogey, D. Juvé, Investigation of Flow Features and Acoustic Radiation of a Round Cavity, AIAA Paper 2008-2851, 2008.
- [35] D. Mincu, I. Mary, S. Redonnet, Numerical Simulations of the Unsteady Flow and Radiated Noise Over a Cylindrical Cavity, AIAA Paper 2008-2917, 2008.
- [36] N. Desvigne, Bruit rayonné par un écoulement subsonique affleurant une cavité cylindrique: caractérisation expérimentale et simulation numérique directe par une approche multidomaine d'ordre élevé (Noise Radiated by a Cylindrical Cavity Placed in a Subsonic Flow: Experimental Study and Direct Acoustic Computation Via a High-order Multidomain Approach), PhD Thesis, Ecole Centrale de Lyon, 2010.
- [37] Y. Yang, D. Rockwell, K. Lai-Fook Cody, M. Pollack, Generation of Tones Due to Flow Past a Deep Cavity: Effect of Streamwise Length, Technical Report LM-06K055, 2006.
- [38] T. Faure, P. Adrianos, F. Lusseyran, L. Pastur, Visualizations of the flow inside an open cavity at medium range Reynolds numbers, *Experiments in Fluids* 42 (2) (2007) 169–184.
- [39] M. Hiwada, T. Kawamura, I. Mabuchi, M. Kumada, Some characteristics of flow pattern and heat transfer past a circular cylindrical cavity, *Bulletin of the JSME* 26 (220) (1983).
- [40] J. Dybenko, E. Savory, An Experimental Investigation of Turbulent Boundary Layer Flow over Surface-mounted Circular Cavities, CSME Forum, 2006.
- [41] C. Haigermoser, F. Scarano, M. Onorato, Investigation of the flow in a circular cavity using stereo and tomographic particle image velocimetry, *Experiments in Fluids* 46 (3) (2009) 517–526.
- [42] V. Sarohia, Experimental and Analytical Investigation of Oscillations in Flows Over Cavities, PhD Thesis, California Institute of Technology, 1975.
- [43] J. Pereira, J. Sousa, Influence of impingement edge geometry on cavity flow oscillations, *AIAA Journal* 32 (8) (1994) 1737–1740.
- [44] J. Bell, R. Mehta, Development of two-stream mixing layer from tripped and untripped boundary layers, *AIAA Journal* 28 (12) (1990) 2034–2042.
- [45] N. Forestier, L. Jacquin, P. Geffroy, The mixing layer over a deep cavity at high-subsonic speed, *Journal of Fluid Mechanics* 475 (2003) 101–145.
- [46] M. Olsen, J. Dutton, Stochastic estimation of large structures in an incompressible mixing layer, *AIAA Journal* 40 (12) (2002).
- [47] R.D. Blevins, *Formulas for Natural Frequency and Mode Shape*, Krieger Pub. Co, 2001.
- [48] Y. Nomura, I. Yamamura, S. Inawashiro, On the acoustic radiation from a flanged circular pipe, *Journal of the Physical Society of Japan* 15 (3) (1960).
- [49] M. Kegerise, E. Spina, S. Garg, L. Cattafesta, Mode-switching and nonlinear effects in compressible flow over a cavity, *Physics of Fluids* 16 (3) (2004) 678–687.
- [50] H. Heller, D. Bliss, The Physical Mechanism of Flow-induced Pressure Fluctuations in Cavities and Concepts for Their Suppression, AIAA Paper, No. 75-491, 1975.

- [51] J. Malone, M. Debiasi, J. Little, M. Samimy, Analysis of the spectral relationships of cavity tones in subsonic resonant cavity flows, *Physics of Fluids* 21 (055103) (2009) 1–9.
- [52] T.D. Mast, A.D. Pierce, Describing-function theory for flow excitation of resonators, *Journal of the Acoustical Society of America* 97 (1) (1995) 163–172.
- [53] A. Michalke, On spatially growing disturbances in an inviscid shear layer, *Journal of Fluid Mechanics* 23 (3) (1965) 521–544.
- [54] A. Norris, I. Sheng, Acoustic radiation from a circular pipe with an infinite flange, *Journal of Sound and Vibration* 135 (1) (1989) 85–93.
- [55] A. Goldman, R. Panton, Measurement of the acoustic impedance of an orifice under a turbulent boundary layer, *Journal of the Acoustical Society of America* 60 (6) (1976) 1397–1404.
- [56] X. Sun, X. Jing, H. Zhang, Y. Shi, Effect of grazing-bias flow interaction on acoustic impedance of perforated plates, *Journal of Sound and Vibration* 254 (3) (2002) 557–573.
- [57] D. Ronnenberger, The acoustical impedance of holes in the wall of flow ducts, *Journal of Sound and Vibration* 24 (1) (1972) 133–150.
- [58] A.K.M.F. Hussain, W.C. Reynolds, The mechanics of an organized wave in turbulent shear flow, *Journal of Fluid Mechanics Digital Archive* 41 (02) (1970) 241–258.
- [59] J. Rayleigh, *The Theory of Sound*, vol. II, revised ed., Dover Publications, New York, 1945.
- [60] L. East, Aerodynamically induced resonance in rectangular cavities, *Journal of Sound and Vibration* 3 (1966) 277–287.